Regular article
First revision
Word count 6601 through Acknowledgments

THERMAL EXPANSION OF MINERALS IN THE TOURMALINE SUPERGROUP

Guy L. Hovis

Department of Geology and Environmental Geosciences, Lafayette College,

Easton, PA 18042

hovisguy@lafayette.edu

Mario Tribaudino

Dipartimento di Scienze della Terra

Università di Torino

Via Valperga Caluso, 35

I-10124 Torino, Italy

mario.tribaudino@unito.it

Caitlin Altomare

Shell Exploration & Production Company (SEPCO), One Shell Square - 701 Poydras Street, New

Orleans, LA 70139

caitlin.altomare@shell.com

Ferdinando Bosi

Dipartimento di Scienze della Terra, Sapienza Università di Roma,

Piazzale Aldo Moro 5. 00185 Rome, Italy

ferdinando.bosi@uniroma1.it

This is the peer-reviewed, final accepted version for American Mineralogist, published by the Mineralogical Society of America.
The published version is subject to change. Cite as Authors (Year) Title. American Mineralogist, in press.
DOI: https://doi.org/10.2138/am-2022-8580. http://www.minsocam.org/

ABSTRACT

The thermal behavior of fifteen natural tourmaline samples has been measured by X-ray powder diffraction from room temperature to ~930 °C. Axial thermal expansion is generally greater along the **c** crystallographic axis ($\alpha_{\mathbf{c}}$ 0.90-1.05 x 10^{-5}/K) than along the **a** crystallographic axis and the symmetrically equivalent **b** axis ($\alpha_{\mathbf{a}}$ 0.47-0.60 x 10^{-5}/K). Ferro-bearing samples show lower expansion along **a** than in other tourmalines. In povondraite the thermal expansion along the **c** axis is higher than in other tourmalines, whereas along **a** it is lower [$\alpha_{\mathbf{a}}$ = 0.31(2) and $\alpha_{\mathbf{c}}$ = 1.49(3) x 10^{-5}/K]. Volume expansion in the tourmaline-supergroup minerals is relatively low compared with other silicates such as pyroxenes and amphiboles. Volume also exhibits a relatively narrow range of thermal expansion coefficients (1.90-2.05 x 10^{-5}/K) among the supergroup members. An interpretation for the small changes in thermal expansion in a compositionally heterogeneous group like tourmaline is that all members, except povondraite, share a framework of dominantly $^{Z}AlO_6$ polyhedra that limit thermal expansion. Povondraite, with a framework dominated by $^{Z}Fe^{3+}O_6$ polyhedra, displays thermal expansion that is different from other members of the group.

Unit-cell dimensions of tourmalines having significant Fe^{2+} deviate from linearity above 400 °C on plots against temperature (T); along with the resulting substantial reduction in unit-cell volume, these effects are likely the result of deprotonation/oxidation processes. Lithium-rich and Fe^{2+}-free tourmalines deviate similarly at T > 600 °C or more. In Li- and Fe^{2+}-free tourmalines no such deviation is observed up to the highest temperatures of our experiments. It is not clear whether this is due to cation order-disorder over *Y* and *Z* sites that occurs during the highest temperature measurements, a phenomenon that is apparently inhibited (at least in the short term) in Li-free/Mg-rich samples. If so, this must occur at a relatively rapid rate, as no difference in unit-cell values was detected at 800 °C after heating in both one- and twelve-hour experiments on Na-rich rossmanite.

This is the peer-reviewed, final accepted version for American Mineralogist, published by the Mineralogical Society of America.
The published version is subject to change. Cite as Authors (Year) Title. American Mineralogist, in press.
DOI: https://doi.org/10.2138/am-2022-8580. http://www.minsocam.org/

Keywords: tourmaline, thermal expansion, modeling, systematics, unit-cell data

INTRODUCTION

In recent papers published in this journal we have explored the thermal expansion of minerals in the pyroxene (Hovis et al. 2021) and amphibole (Tribaudino et al. 2022) mineral supergroups. The present contribution extends this work to minerals of the tourmaline supergroup with the presentation of volume - temperature (V-T) data for fifteen mineral specimens in this supergroup (Altomare 2014, Altomare and Hovis 2014). We have restricted our work to natural tourmaline specimens that could readily be obtained from the U.S. National Museum of Natural History, as well as from two individuals with expertise on tourmaline minerals, Frank Hawthorne and George Rossman.

Relatively recent detailed discussions of the chemical variation and structures of tourmaline minerals have been given by Henry et al. (2011) and Bosi (2018). Minerals of this group are so-called cyclosilicates because of their six-membered ditrigonal rings of tetrahedra, whose presence are reflected well by tourmaline external morphology and also by the overwhelming majority of naturally occurring tourmaline specimens that usually have space-group type *R*3*m* symmetry. Even so, it will be seen that a crucial feature of the tourmaline structure is the arrangement of its ZO_6 polyhedra (Figs. 1a,b; Bosi 2018). A distinctive chemical feature of these minerals is the presence of $(BO_3)^{3-}$ borate groups that make tourmaline a major source of boron.

The general chemical formula for tourmaline-supergroup minerals is $XY_3Z_6T_6O_{18}(BO_3)_3V_3W$ in which $O = O^{2-}$ and $B = B^{3+}$. Occupants of the various crystallographic sites are: $X = Na^{+}$, K^{+}, Ca^{2+}, □ (= vacancy); $Y = Al^{3+}$, Fe^{3+}, Cr^{3+}, V^{3+}, Fe^{2+}, Mg^{2+}, Mn^{2+}, Li^{+}, Ti^{4+}; $Z = Al^{3+}$, Fe^{3+}, Cr^{3+}, V^{3+}, Mg^{2+}, Fe^{2+}; $T = Si^{4+}$, Al^{3+}, B^{3+}; $V = (OH)^{-}$, O^{2-}; and $W = (OH)^{-}$, F^{-}, O^{2-} (Henry et al. 2011; Bosi 2018). Paraphrasing from Bosi (2018), the nine-coordinated XO_9 antiprism and T_6O_{18} ring combine with two sets of three octahedra YO_6; a $[Y_3O_{15}]$ triplet of octahedra caps the XO_9 polyhedron toward the +**c** axis, with the

other [Y_3O_{12}] capping the [T_6O_{18}] ring of tetrahedra toward the –**c** axis. The BO_3 groups are oriented sub-parallel to (0001) and lie between the rings of tetrahedra. The structural arrangement of [T_6O_{18}], XO_9, [Y_6O_{18}], and $(BO_3)_3$ form "islands" that are stacked in columns along the **c** axis. These islands are attached to one another along the **a** and **b** crystallographic axes by spiral chains of ZO_6 octahedra, which also extend along the **c** axis via a 3_1 triad screw axis. The three-dimensional framework of the tourmaline structure is therefore given by the screw-like arrangement of ZO_6. Figures 1a,b illustrate the cations at the *X*, *Y*, *B* and *T* sites located in the channels formed by the ZO_6 polyhedral arrangement. This framework is very stable and explains some physical properties such as hardness (~7–7.5 Mohs scale) and extensive pressure-temperature stability (up to about 7 GPa and 950 °C) of tourmaline (e.g., Dutrow and Henry 2011; Bosi 2018). Recently, Berryman et al. (2019) showed that the framework provided by ZO_6 exerts a primary control on the compressibility of tourmalines. The structural complexity and extensive chemical substitution in this system provide the possibility for a large number of tourmaline end members, all of which have been noted in the two publications above.

Relatively few in-situ high temperature investigations on the thermal expansion of tourmaline have been done. Preliminary investigation by Libermann and Gandall (1952) showed thermal expansion that is almost double along the c relative to the **a** crystallographic axis, specifically 0.4 vs. 0.9×10^{-5}/K, as confirmed by several subsequent investigations (Filatov et al. 1987; Tatli and Pavlovic1988; Hemingway et al. 1996; Pandley and Schreurer 2012; Watenphul et al. 2017; Chernyshova et al. 2019; Celata et al. 2021; Ballirano et al. 2022). An exception to the previous results is the study of Donnay (1977), who found a volume thermal expansion more than double that of other investigations (α_V = 4.6 vs. 2 $\times 10^{-5}$/K), a result that was later found as well by Xu et al. (2016) in a high-temperature high-pressure synchrotron investigation.

An analysis of the changes in thermal expansion with temperature was undertaken by Filatov et al. (1987) in a high-temperature X-ray investigation conducted up to 900 °C on four tourmalines, three of them Fe^{2+}-rich and one Fe^{2+}-free and Li-rich. The former showed a nonlinear decrease of the a_0

parameter at temperature T > 400 °C with corresponding increases along the **c** axis. This was interpreted to be the result of Fe^{2+} to Fe^{3+} oxidation. This effect was later confirmed, albeit at higher temperature, by the Raman investigation of Watenphul et al. (2017).

The most accurate previous investigation on tourmaline thermal expansion comes from Pandley and Schreurer (2012), who used an inductive gauge dilatometer between 100 and 903 K (–173 to 630 °C) to measure the expansion of five large tourmaline crystals having elbaite-schorl and schorl-dravite compositions. These workers observed higher expansion in Fe^{2+}-free samples. Additionally, they observed a small irreversible softening in elastic parameters in the Li-richer samples.

Despite the valuable work described above, a systematic investigation of a compositionally diverse group of minerals in the tourmaline system by X-ray diffraction, XRD, as a function of temperature, f(T), is lacking. Specifically, we ask (1) how the tourmaline unit cell is affected by temperature and (2) how the latter varies as a function of chemical composition. Additionally, we ask (3) how the high-T behavior of tourmaline is affected by effects (e.g., oxidation and deprotonation) other than chemical composition and (4) how present thermal expansion data are best described by various thermal expansion models. Here we report on the thermal expansion of fifteen different tourmalines. Relative to dilatometric methods, present work has not been restricted to the study of gem-quality crystals, which has allowed investigation of a relatively wide range of composition.

EXPERIMENTAL

Samples investigated

Given the chemical complexity and structural constraints of this mineral supergroup (e.g., Bosi 2018), it would have been difficult to obtain every existing tourmaline end member or near-end-member for this investigation. Rather, our approach was to obtain available samples from museum collections or individuals who have been involved in tourmaline research, with the requirement that we

would need samples for which chemical information was available. We also attempted to investigate a sufficiently wide range of composition that would make it possible to understand how this system operates structurally at high T. Because of chemical zoning that is common for minerals in this system, we attempted to avoid such samples; the exceptions to this are (1) fluor-schorl sample T21 (which produced only slightly broadened XRD peaks) and (2) povondraite (which generally produced grossly widened peaks). Because povondraite proved to be chemically inhomogeneous, we obtained samples from three different sources (American Museum of Natural History, Mineralogical and Geological Museum at Harvard University, and Frank Hawthorne) in the hopes of finding a relatively homogeneous sample. Because the Harvard sample was very small relative to the others, it showed less inhomogeneity, but even it proved to be compositionally problematic.

Names, sources, and chemical compositions of investigated samples are listed in Table 1. In addition to sample names provided by the various sources, we also give in Table 1 sample names based on the classification scheme of Henry et al. (2011), which is used throughout this paper. NMNH samples were analyzed by methods found in Dunn et al. (1977). Analyses of specimens obtained from George Rossman were made using techniques described by Ma et al. (2012). Samples obtained from Frank Hawthorne (personal communication) were analyzed using a CAMECA SX-50 electron microprobe in wavelength-dispersive mode. Beam voltage for all elements was 15 KV and spot diameter was 1 μm. Count times for peak background determinations for all elements were 20 and 10 s, respectively. Data were collected with a beam current of 20 nA for Na, Fe, Ca, Al, Si, and Mg and 30 nA for F, Cr, V, Mn, Zn, K, Ti, and P.

Povondraite chemical analyses

Electron-microprobe analyses of povondraite sample 110379 from the American Museum of Natural History were obtained by wavelength-dispersive spectrometry (WDS mode, 15 kV, 15 nA, 10 μm beam diameter) with a Cameca SX50 instrument (CNR-Istituto di Geologia Ambientale e

Geoingegneria, Roma, Italy). The following standards, X-ray *K*α lines and analyzer crystals were used: jadeite (Na; TAP), periclase (Mg; TAP), orthoclase (K; PET), rutile (Ti; PET), wollastonite (Si, Ca; PET), metallic Zn and Mn (Zn, Mn; LIF), vanadinite (V; PET), fluorophlogopite (F; TAP), metallic Cr (Cr; PET), corundum (Al; TAP), magnetite (Fe; LIF). The "PAP" routine was applied (Pouchou and Pichoir 1991). The results (Table 2) represent mean values of 117 spot analyses across several crystals. This povondraite sample was also analyzed by ^{57}Fe Mössbauer spectroscopy (Swedish Museum of Natural History, Stockholm, Sweden) using a conventional spectrometer system operated in constant-acceleration mode. The Mössbauer spectrum indicates the presence of only Fe^{3+}. This chemical analysis resulted in the empirical formula:

$^{X}(Na_{0.81}K_{0.22}Ca_{0.01})_{\Sigma 1.04}\,^{Y}(Fe^{3+}_{2.92}Ti_{0.03})_{\Sigma 2.96}\,^{Z}(Fe^{3+}_{3.55}Mg_{1.74}Al_{0.72})_{\Sigma 6.00}\,^{T}(Si_{6.05}O_{18})\,(BO_3)_3\,^{V}[(OH)_{2.59}O_{0.39}]$ $^{W}(O_{0.98}F_{0.02})_{\Sigma 1.00}$. The (OH) content and the atoms per formula unit (apfu) in the formula were calculated by charge balance assuming B = 3.00 apfu, cation at ($T + Y + Z$) = 15 apfu and 31 anions pfu. Further details of povondraite will be published in a separate paper.

X-ray diffraction

X-ray powder diffraction measurements were conducted from room T to ~928 °C at mostly 50 °C intervals on a PANalytical Empyrean X-ray powder diffraction system equipped with an Anton-Parr HTK 1200N heating stage. Scans covering a 2Θ range of 15° to 80° took place over a 30 min time period. Actual sample temperatures were checked through independent experiments on several compounds that display second-order phase transitions, as described in detail by Hovis et al. (2021). Generally, observed temperatures of our experiments were found to be 16 °C to 28 °C above the set temperature displayed on the controller console. This range in temperature correction probably does not represent real variation in instrumental vs. actual T (ΔT), but likely reflects the standard deviation in average ΔT values that became evident only after ever-increasing experience with the new XRD system over an extended period of time. During data reduction, unit-cell calculations utilized adjusted

sample peak positions that employed NIST (NBS) 640a silicon as an internal standard. Extended discussion of XRD methodology and unit-cell calculation is given on pp. 884-885 of a previous paper on pyroxene thermal expansion (Hovis et al. 2021).

At the conclusion of all XRD experiments a room-T X-ray scan was conducted to check for possible sample breakdown due to dehydration and/or Fe oxidation. During data reduction of each tourmaline sample, however, it was not unusual to note broadening and in some cases loss of intensity in X-ray peaks (or even obvious loss of the tourmaline XRD pattern) at some point during sample heating, although the temperature at which such deterioration began varied from sample to sample. The latter accounts for the reason why so few unit-cell dimensions were determined for samples of the post-heating room-T XRD experiments (see Table OM1). Sample changes also were indicated by off-trend unit-cell dimensions with increasing T. In addition, for Fe^{2+}-bearing tourmalines it was common to note changed color to rusty-red or brown by the conclusion of an experiment. In the end, most of the tourmaline specimens that we investigated produced data that were affected by some sort of chemical change below the maximum ~930 °C temperature of our experiments. Many samples, however, did produce high-quality data over extensive temperature ranges, some as high as 878 °C, as reflected by the data reported in supplemental Table OM1 and shown in supplemental Figure OM1.

Unit-cell dimensions were calculated using the X-ray software of Holland and Redfern (1997). To avoid the automated indexing of X-ray peaks that were the result of phase impurities (e.g., natural quartz in the sample or corundum peaks from the sample holder), the *hkl* identities of all peaks were assigned manually, for which both the *American Mineralogist* Crystal Structure Database (Downs and Hall-Wallace 2003) and PANalytical Database were invaluable. Because of this manual indexing, rather than automated indexing available on various XRD systems, we regard the stated standard errors of our computed unit-cell dimensions to be realistic. The wavelength of Cu$K\alpha_1$ radiation for all calculations was taken to be 1.540598 Å, which was the value inherent in PANalytical software; peaks from Cu$K\alpha_2$ radiation were stripped during data reduction. Note that the significantly lower precision

of calculated unit-cell dimensions for the three povondraite specimens (supplemental Table OM2 and Fig. OM2) is both the result of broad XRD peaks produced by substantial chemical zoning as well as unit-cell dimensions necessarily based only on relatively low-2Θ (high-*d*) peaks.

To assess the effect of changes during repeated heating cycles, whether for sample deterioration or cation order, we also performed a series of repeated heating experiments in order to achieve elevated temperatures at different rates. These experiments were repeated three times on sample GRR 916 Na-rich rossmannite (formerly elbaite), using for each run a new batch of grains. For the first experiment, having "normal" ~50 °C intervals, XRD run time at each T was 30 min with heating and thermal equilibration times between temperatures of 8 to 9 min, for a total run time of an up-temperature set of experiments of about 12 h. For the second set of experiments having 200 °C intervals, heating and equilibration time between temperatures was ~24 min and XRD time 30 min, with a total run time for the up-temperature set of experiments of about 4 h. The third experiment involved just three measurements, one at room T, and two at 800 °C. Heating and thermal equilibration time between room-T and 800 °C was ~23 min, followed by a 30-min XRD measurement. Following the latter, a second 30-min XRD experiment was performed after a wait time of 30 min. For all three sets of experiments room-temperature XRD data were collected after cooling. As shown in supplemental Figure OM2, the results from these experiments (given in supplemental Table OM2) are fully comparable, which demonstrates (at least for this sample) that thermal behavior is unaffected by heating rate.

RESULTS

The calculated unit-cell dimensions for most tourmaline samples are presented as a function of temperature in supplemental Table OM1 and Figure OM1; because of chemical inhomogeneity, those for the three povondraite samples are reported separately in supplemental Table OM2 and Figure OM2. Reported standard errors from the Holland and Redfern (1997) software represent 1σ values; these

should be multiplied by a factor of 2 or 3 to obtain a more realistic estimate of data uncertainty. A sample plot of the refined unit cell is shown in Figure 2.

Data analysis: Fitting the thermal expansion data

Thermal expansion data can be fit with either physical or empirical models. Such models were used together in recent investigations on pyroxenes and amphiboles (Hovis et al. 2021; Tribaudino et al. 2022), whereas in most papers either empirical (e.g., in plagioclase Hovis et al. 2010, Tribaudino et al. 2010, in pyroxenes Pandolfo et al. 2015) or physical models (e.g., in plagioclase Tribaudino et al. 2011, in olivine Kroll et al. 2012, in pyroxene Knight et al. 2008, in amphibole Tribaudino et al. 2008) were used exclusively. Physical models are generally preferable, as they link thermal expansion to basic properties such as vibrational energy and bulk modulus. However, such models are highly demanding in terms of data quality. A critical quantity is the first derivative of volume with respect to temperature, i.e., thermal expansion. While the latter generally changes little above room temperature (commonly approximated as constant over a limited T range as shown in Fig. 3), changes below room-T are normally quite significant (Tribaudino et al. 2012). It is especially helpful, then, if both low- and high-T volume data are collected. For the tourmaline supergroup, to our knowledge, unit-cell dimensions have not previously been determined below room T; however, thermal expansion between 80 and 300 K has indeed been measured by dilatometric methods in two papers (Tatli and Pavlovic 1988; Pandley and Scheurer 2012) on elbaitic, schorlitic, uvitic and dravitic samples. Although present tourmalines have different compositions (and thermal expansions) than samples in the cited papers, we have taken the liberty of merging the low-T data for several of the latter samples with those of compositionally comparable specimens studied here, which provides the basis for a physical fit to the combined data.

To analyze the combined data, we have utilized the Kroll equation (see Angel et al. 2014), which includes four refinable parameters, V_{298K}, α_{298}, θ_E, K', i.e., the unit-cell volume, thermal

expansion coefficient at 298 K, Einstein temperature and first derivative of the bulk modulus. While the first two of these parameters are usually refined, at least one, either θ_E and or K', must be fixed in order to constrain the refinement. For the present case we have fixed K' at a value of 4, which corresponds to the approximation of a second-order truncation in the Birch-Murnaghan equation of state. This is based on the investigation by Berryman et al. (2019), who found K' values very close to 4 in their systematic analysis of tourmaline at high pressure. The low-temperature dilatometric thermal expansion was fit to room-temperature unit-cell volume to calculate fictive unit cells below room temperature. Refined values of θ_E, V_{298K} and α_{298} are reported in Table 3. As a sample plot volume thermal expansion with temperature is shown for Na-rich rossmanite and schorl in Figure 3.

As low-temperature expansion data are available for only a few samples, we have also fit our data above room-T also with an empirical equation, namely that of Fei (Angel et al. 2014):

$V = V_0 \exp[a_0(T - T_{ref}) + 1/2a_1(T^2 - T_{ref}^2) - a_2(1/T - 1/T_{ref})]$.

In the latter there are four refinable parameters, V_0, a_0, a_1 and a_2, with V_0 the volume at reference temperature 298 K. In this calculation refinements that included the a_2 parameter did not produce values higher than the error, so the equation was truncated at the quadratic term. As discussed below, the range of data included in the fit turned out to be critical as a result of changes in tourmaline crystal chemistry induced by heating (Figs 4 and 5). Resulting refined parameters overstated temperature ranges are reported in Table 4.

Povondraite thermal expansion

As noted above, the chemical inhomogeneity of povondraite (shown by the high standard deviation values of Fe^{3+} and Al in Table 2) causes relatively high dispersion in unit-cell data, as reflected by supplemental Table OM2 and Figure OM2. This also is shown by the relatively large standard deviations of calculated unit-cell dimensions for all povondraite samples, which are necessarily based on just seven peaks that occur between 17° and 35° 2Θ. When compared with the

This is the peer-reviewed, final accepted version for American Mineralogist, published by the Mineralogical Society of America.
The published version is subject to change. Cite as Authors (Year) Title. American Mineralogist, in press.
DOI: https://doi.org/10.2138/am-2022-8580. http://www.minsocam.org/

XRD data for relatively homogeneous tourmalines such as □-rich dravite NMNH 78719-1, Na-rich rossmanite GRR 916, and fluoruvite NMNH B14687, average 2Θ peak widths at half-maximum for the seven peaks are 1.5, 2.3, and 2.5 times greater for the Harvard, AMNH, and Hawthorne samples, respectively, than for the more homogeneous samples. The narrower peak widths for the Harvard sample also correlate nicely with smoother systematic variability of unit-cell dimensions as f(T) in Figure OM2 as well as the very small size of that sample.

The unit-cell data confirm that povondraite shows a markedly higher expansion along the **c** axis than do other tourmalines, also "steplike" behavior for the *a* parameter as f(T); the latter is shown as an increase in *a* up to 350 °C (similar to that of dravite and other tourmalines), then a flattening in variability between 350 and 500 °C, then another increase above 500 °C but at a rate lower than that for dravite (Fig. 6). Decomposition occurs only at T higher than 700 °C. Unlike other tourmalines, this cannot be ascribed to oxidation of Fe^{2+} to Fe^{3+}, as all original iron is already ferric.

DISCUSSION

High temperature decomposition: deprotonation and intra-crystalline disorder

Thermal expansion in solids is an effect of anharmonic terms in the potential energy on the mean separation of atoms at a temperature, which generally causes volume to increase with temperature (Kittel et al. 1996, pp.104-130). Generally, samples are assumed to be structurally and chemically homogeneous. If at high temperature other volume-changing processes occur (e.g., dehydration-deprotonation, oxidation, phase transitions, cation disorder), these must be taken into account, as such processes may affect unit cell parameters (e.g., Filatov et al. 1987).

A critical issue in measuring thermal expansion is the selection of high-temperature data to include in such analyses for phases that undergo high-temperature alteration. In the case of V-T data it is important to critically evaluate trends for unusual deviation(s) from the norm. For present data, we find that up to 400 °C there is little deviation from almost-linear V-T trends. At higher temperatures,

however, Fe^{2+}-rich tourmalines show breakdown or significant deviation from lower-temperature trends (Fig. 4). Moreover, some samples show differences in room-T unit-cell parameters pre- vs. post-heating. A gross such example is shown by the room-T unit cells of Na-rich foitite measured "after" vs. "before" heating, which show a decrease by 0.115 Å in *a*, an increase of 0.013 Å in *c*, and an overall decrease in volume of 19.8 $Å^3$ (see Table OM1). The behavior of Fe^{2+}-rich tourmalines has been ascribed to oxidation and deprotonation, where deprotonation has the effect of decreasing both the *a* unit-cell parameter and volume (Pieczka and Kraczka 2004; Filip et al. 2012; Bosi et al. 2018, 2019) due to the smaller size of Fe^{3+} vs. Fe^{2+}.

Also, intracrystalline cation disorder may affect the variation of the unit-cell parameters, because both *a* and *c* are related respectively to the size of cations at the *Y* and *Z* sites (e.g., Bosi et al., 2010). This strict dependence may be explained by the plane of triads of edge-sharing YO_6 octahedra that is parallel to the **a**-axis, whereas the arrangement of spiral chains of ZO_6 polyhedra around the 3_1 axis is parallel to the **c**-axis. Any intracrystalline disorder reaction $^{Y}R + {}^{Z}Al = {}^{Y}Al + {}^{Z}R$ (where R represents a generic cation), therefore, will reduce *a* and increase *c*, as Al is the smallest [6]-fold coordinated cation occurring in the tourmaline structure (Bosi 2018).

In general, the unusual unit-cell variations from the norm should be related to iron oxidation/deprotonation (which normally occur at *Y* and in turn decrease the *a* parameter) and to the cation order-disorder $^{Y}Fe + {}^{Z}Al = {}^{Y}Al + {}^{Z}Fe$ (which decrease the *a*-parameter and increase the *c*-parameter).

Intracrystalline cation disorder likely affects some Li-rich tourmalines. In Figure 5 we compare unit-cell edges (*a* and *c*) and volumes observed in elbaite and Na-rich rossmanite with the thermal expansion modeled by Pandley and Schreurer (2012) in an elbaitic sample, based on their low temperature data. Assuming that the trend by these workers solely represents thermal expansion, as it is based on low-temperature data where the cited processes that may affect the unit-cell values are inhibited, there is good agreement between present data and the low-high temperature dilatometric data

up to 800 K. At higher temperatures, however, one observes in present samples lower values for the *a* parameter, but higher expansion along **c**. The resulting volume shows a slightly lower value relative to that predicted by the Pandley and Scheurer (2012) fit. The *a* parameter is lower in FH AT31 elbaite, which is Fe-bearing, compared to the GRR 916 Na-rich rossmanite, which is Fe-free (Table 1). Thermal expansion for elbaite has also been provided by Hemingway et al. (1996), who noted two different thermal expansion rates below vs. above 500 °C (773 K), the latter lower for the *a* parameter but higher for *c*. The effect is amplified between 850 and 940 °C, where *a* shows a decrease of 0.026 Å and *c* an increase of 0.023 Å, compared with increases of 0.047 and 0.074 Å for *a* and *c*, respectively, between room T and 850 °C. This suggests that in these tourmalines thermal behavior is the result of an additional mechanism besides thermal expansion, likely related to irreversible elastic softening observed by Panday and Schreurer (2012) following their first heating run. This seems to be consistent with Ballirano et al. (2022) (see Fig. 2) who explained the observed structural variations in elbaite by intracrystalline order-disorder reactions involving disorder $^{Y}Li + {}^{Z}Al = {}^{Y}Al + {}^{Z}Li$ at T higher than 750 °C. Hemingway et al. (1996) also found a similar trend.

If related to cation ordering the response might be significantly different in different tourmalines: in the Na-rich rossmanite and elbaite samples in Figure 5 we find higher deviation in the Fe-bearing FH AT31 elbaite, and a much higher response at lower temperature for the *a* parameter and to a higher extent for *c*, in the Ballirano et al. (2022) elbaite. Also, the effect on unit-cell parameters that we might expect in runs with different heating rates and duration, was not found in Fe-free Na-rich rossmannite, where runs lasting from 1 to 12 hours gave the same unit cell values (Table and Fig. OM3). The suggestion is that the intracrystalline disordering process might have occurred at a rather fast rate.

Axial and volume thermal expansion

This is the peer-reviewed, final accepted version for American Mineralogist, published by the Mineralogical Society of America.
The published version is subject to change. Cite as Authors (Year) Title. American Mineralogist, in press.
DOI: https://doi.org/10.2138/am-2022-8580. http://www.minsocam.org/

In Figure 4 we show the thermal expansion results from present work on all tourmalines except povondraite. Three different compositional groups are present, in terms of decomposition temperature and more or less pronounced deviation from a linear behavior. We have: (1) Fe^{2+}-rich tourmalines that show lower thermal expansion and decompose at lower temperature, (2) Li-rich tourmalines that follow an almost linear expansion along **c** up to 400 °C before deviating (in a more or less pronounced manner) from a linear trend, and (3) tourmalines with negligible Li and Fe^{2+} (Li-Fe^{2+}-free) that show closer to linear behavior between unit-cell parameters and T up to the beginning of decomposition at ~950 °C. Fluor-liddicoatite divides groups 2 and 3.

Fits done using the empirical Fei equation (Table 4) show that the *a* parameter expands almost linearly. The a_1 parameter in the Fei expansion is barely significant, and in fluor-buergerite is slightly negative, which would indicate that thermal expansion along **a** decreases somewhat with temperature. Because fluor-buergerite is (OH)-free and the unit-cell parameters measured in fluor-buergerite after heating are within 3σ of those before the run, we suggest that the disorder reaction $^{Y}Fe^{3+} + {}^{Z}Al = {}^{Y}Al + {}^{Z}Fe^{3+}$ is negligible in this sample. Along the **c** axis thermal expansion increases significantly with temperature, with the a_1 parameter always significant.

For present samples, room-T thermal expansion coefficients along **a** have been plotted against those along **c** (Fig. 7). Additionally, Figure 8 shows volume thermal expansion coefficients plotted against those for the **a** axis. Noting the different designations for the three tourmaline groups (Fe^{2+}-rich, Li-rich and Li-Fe^{2+}-free), it appears that the Fe^{2+}-rich tourmalines do show lower thermal expansion than the others, and Fe^{2+}- and Li-rich tourmalines have lower expansivity along **c** than the Li and Fe-free tourmalines; this suggests that Fe and/or Li presence may inhibit thermal expansion along **c**. An exception is NMNH B14687 fluor-uvite, which shows a lower thermal expansion, even though it is Li-Fe^{2+}-free (Table 1). In volume, we see an almost linear behavior between volume and expansion along the **a** axis (Fig. 8), with Fe^{2+}-rich tourmalines showing lower expansion.

Present results can be compared with previous observations among various tourmaline species. Tatli and Pavlovic (1988) observed that uvitic, schorlitic and elbaitic tourmalines show progressively higher expansion. Present work indicates Fe-free fluor-uvite (sample NMNH B14687) has greater expansion than schorl, close to that of elbaite, whereas Fe-rich fluor-uvite (sample FH T95/CT72) shows expansion similar to schorl but less than elbaite. Pavlov and Scheurer (2012) showed that Li-rich tourmalines exhibit higher expansion than Li-free ones, although this is not observed in present data. Only fluor-liddicoatite shows a (slightly) higher expansion than dravite, whereas elbaitic samples do not.

Perhaps most importantly, current work indicates that thermal expansion is similar among different tourmalines, ranging from higher volume expansion for fluor-buergerite and fluor-liddicoatite (2.2×10^{-5}/K) to lower expansion for schorl (1.9×10^{-5}/K). This constitutes a remarkably small range of thermal expansion coefficients relative to the chemical diversity exhibited by this supergroup of minerals. Comparatively, plagioclase feldspar thermal expansion varies between 2.5×10^{-5}/K in albite and 1.0×10^{-5}/K in anorthite (Tribaudino et al. 2010). Pyroxene supergroup expansion ranges from 1.8×10^{-5}/K for kosmochlor to 3.0×10^{-5}/K for hedenbergite (Hovis et al. 2021). Amphibole coefficients vary between 1.6×10^{-5}/K for a synthetic amphibole to 3.2×10^{-5}/K for anthophyllite (Tribaudino et al. 2022) (Fig. 9).

What might account for the narrow range of thermal expansion coefficients exhibited across the tourmaline supergroup? We suggest that there may be a simple crystal-chemical explanation. Note first that Al (mainly at the *Z* site, but also at the *Y* site), Si (at the *T* site) and B (at the *B* site) dominate the chemical compositions of presently investigated tourmalines, except povondraite. Apart from (OH) groups, other "secondary" constituents that define the various mineral species occupy *Y* and *X* sites. Overall, then, the structure may be viewed as a 3D framework of $^{Z}AlO_6$ polyhedra (Fig. 1a,b) that encloses structural islands made up of X-Y-T-B polyhedra (Bosi 2018). Perhaps the thermal behavior

398 of tourmaline is largely independent of composition simply because all structures are dominated by this
399 3D $^{Z}AlO_6$ framework.

400 Interestingly, similar thermal expansion coefficients have been found in Al-pyroxenes and
401 analogue amphiboles, e.g., jadeite and glaucophane, showing respectively $\alpha_V = 2.1$ and 2.4×10^{-5}/K. In
402 these phases too octahedral polyhedra dominate thermal expansion (Tribaudino and Mantovani 2014;
403 Hovis et al. 2021), with the smaller polyhedron occupied by Al^{3+} showing stronger bonding with
404 oxygen and thus reduced thermal expansion.

405 The thermal expansion of povondraite, where Fe^{3+} exchanges for Al, could challenge this
406 suggestion. In fact, the axial thermal expansion of povondraite is significantly different from other
407 tourmalines, with higher expansion along the **c** axis, but lower along **a**, which could reflect a strong
408 increase of ^{Z}Fe compensated by an increase of ^{Y}Al according to the intracrystalline reaction $^{Y}Fe^{3+} + {}^{Z}Al$
409 $= {}^{Y}Al + {}^{Z}Fe^{3+}$. However, as shown in Figure 6, the volume is very close to that of dravite. The missing
410 expansion in povondraite between 350 and 500 °C could be related to some yet unidentified process
411 that lowers the thermal expansion along the **a** axis from the value it should have.

412 As for axial thermal expansion, that along the **c** axis is almost twice the expansion on (001) in
413 the studied tourmalines. That thermal expansion is greater along **c** than **a** is consistent with the elastic
414 constant values reported by Pandey and Schreuer (2012), where the longitudinal stiffness parallel to
415 the **c**-axis (c_{33}) is smaller than that parallel to **a** (c_{11}). This indicates that atomic bonding along the **c**-
416 axis is weaker than that within the (001) plane (along the **a**-axis). Structurally, this suggests that the
417 spiral chains of the $^{Z}AlO_6$ polyhedra can "easily" elongate around the 3_1 triad screw axis (parallel to the
418 **c** crystallographic axis), whereas expansion of the structure along the **a** axis, where the structural
419 islands are located, is more difficult. This structural expansion may be enhanced by the substitution of
420 ^{Z}Al (a hard cation) by ^{Z}Fe (a softer cation) such as occurs in povondraite. It is noteworthy that
421 Berryman et al. (2019) have given a similar interpretation to tourmaline compressibility.

422

This is the peer-reviewed, final accepted version for American Mineralogist, published by the Mineralogical Society of America.
The published version is subject to change. Cite as Authors (Year) Title. American Mineralogist, in press.
DOI: https://doi.org/10.2138/am-2022-8580. http://www.minsocam.org/

Compression and thermal expansion: An inverse behavior?

Berryman et al. (2019) studied the high-pressure behavior in several synthetic tourmalines. These workers found that compression along the **c** axis is about three times that along the **a** axis, which mirrors the higher thermal expansion along **c** axis, and almost twice that along **a**. Moreover, Berryman et al. (2019) provide a compilation of tourmaline bulk moduli calculated from different experimental sources. Just as found here for thermal expansion, one observes relatively close values among the reported tourmaline members, with the ten reported bulk moduli for elbaite and schorl from different sources (Helme and King 1978; Tatli and Ozkan 1987; Panday and Schreurer 2012), either pure or in reciprocal solid solution with dravite, between 114 and 121 GPa. Recent data on synthetic dravite, K-dravite, oxy-uvite (actually magnesio-lucchesiite; Scribner et al. 2021), magnesio-foitite and olenite by Berryman et al. (2019) show lower (but comparable) values between 109 and 116 GPa. In addition, high-pressure behavior seems to show little variability despite tourmaline composition. Berryman et al. (2019) do report an exception for olenite (an Al-dominant tourmaline), which shows a lower compressibility along the **c** axis. Among present samples, the □-Al-B rich elbaite (previously called olenite) is compositionally closest to the Berryman et al. (2019) olenite; it shows a lower thermal expansion along the **c** axis than other tourmalines (Table 3). This indicates that the deformation along the **c** axis, either for thermal expansion or compression, is more difficult in olenite than in other tourmalines, perhaps due to the presence of Al^{3+} at both *Y* and *Z* sites that increases the *Y*-O and *Z*-O Pauling bond-strength up to 0.5 valence units relative to a bond strength for divalent cation occupancy of about 0.33 valence units.

In addition, the few data points on Fe-free dravite suggest a higher compressibility than other tourmalines (Fig. 5 and 6 of Berryman et al. 2019), mostly along the **c** axis. Here a higher compressibility is mirrored by the higher thermal expansion we have found in this investigation.

IMPLICATIONS

448 The tourmaline supergroup of minerals are widespread in Earth's crust, typically occurring in
449 granites and granitic pegmatites, as well as in certain sedimentary and metamorphic rocks (Dutrow and
450 Henry 2011). In addition to their importance as rock-forming minerals in pegmatitic high-temperature
451 rocks, tourmaline-supergroup members are the primary boron-bearing minerals in the earth.
452 Tourmaline thermal-expansion data, therefore, are essential to the thermodynamic modelling not only
453 of pegmatitic environments, but of all high-temperature B-rich mineral assemblages. Here, we provide
454 an updated high-T dataset for the tourmaline mineral supergroup that will serve thermodynamic
455 databases such as Perple X and as well be a valuable tool for better understanding tourmaline physical
456 properties. Overall, present data demonstrate a similarity in thermal expansion among a wide variety of
457 tourmaline compositions; this provides the possibility of using end-member thermal expansion data for
458 compositions that deviate significantly from those studied here.
459 Another implication of present results is the potential utilization of temperature-dependent
460 cation order/disorder to help unravel the kinetics of geological processes pertinent to the environments
461 in which tourmaline occurs. Cation order/disorder has been investigated in a number of other mineral
462 groups, for example: spinel (Redfern et al. 1999; Andreozzi et al. 2000), feldspar (Megaw 1959; Angel
463 et al. 1990, Tribaudino et al. 2018), pyroxene (Ghose 1965, Ganguly et al. 1989, Ganguly and
464 Domeneghetti 1994), and more recently dolomite (Pina et al. 2020). Moreover, worthwhile petrologic
465 information has resulted from the use of order/disorder phenomena. For example, from Fe-Mg ordering
466 in orthopyroxenes the cooling rate in meteorites has been assessed (e.g., Molin et al. 1994). Order-
467 disorder processes also have been used to infer cooling rates of the Skaergaard intrusion (Ganguly and
468 Domeneghetti 1994). Despite such examples, we would argue that the use of this phenomenon as a
469 petrologic tool has been underutilized.
470 We have demonstrated here (Fig. 5) that intracrystalline cation disorder likely affects the
471 tourmaline unit-cell values, especially the *a* parameter but probably *c* as well. This follows the work of
472 Bosi et al. (2016, 2018, 2019), who also have reported thermally induced ionic redistribution in several

tourmaline minerals. One must wonder, then, about the many possible relationships among order/disorder, temperature, kinetics, chemical composition, and oxidation state in this chemically diverse mineral system. Logical next steps in this endeavor might include investigation of the role of Mg and other elements in determining the onset and kinetics of ordering, studies of the kinetics of order/disorder as a function of temperature, and determination of how the oxidation state of a geological environment influences order/disorder. A refined understanding of order/disorder phenomena in the tourmaline system could provide new and important tools for the investigation of various geologic environments in which these minerals occur.

ACKNOWLEDGMENTS

One of the original purposes of this thermal expansion work was to involve undergraduate students at Lafayette College in meaningful research. Participating students have been coauthors of previous thermal expansion papers (Hovis et al., 2021; Tribaudino et al., 2022). One such student who focused largely on thermal expansion in the tourmaline system is coauthor of the present work; those results also have been published as a senior honors thesis at Lafayette College (Altomare 2014) and a Geological Society of America abstract (Altomare and Hovis 2014).

This thermal expansion research would not have been possible without financial support from the U.S. National Science Foundation, Earth Sciences Division, for both the X-ray equipment and student participation via grants EAR-1019809 and EAR-1028953. We are grateful as well for support from the Excel Scholars Program of Lafayette College. A Sapienza University of Rome grant (Prog. Università 2020 to F. Bosi) is also gratefully acknowledged. We could not have done this work without the tourmaline samples so generously contributed by Jeff Post and Paul Powhat (National Museum of Natural History), Frank Hawthorne (University of Manitoba), George Rossman (Caltech), George Harlow (American Museum of Natural History), and Raquel Alonso Perez and Kevin Czaja

(Mineralogical and Geological Museum at Harvard University). Finally, we greatly appreciate the thoughtful reviews of this paper by Eleanor Berryman and Andreas Ertl.

REFERENCES CITED

Altomare, C.M., ms (2014) Thermal expansion in the tourmaline mineral system: Senior Honors Thesis, Lafayette College, Easton, 68 p.

Altomare, C.M., and Hovis, G.L. (2014) Thermal expansion in the tourmaline mineral system. Abstracts of the Northeast Section Meeting of the Geological Society of America, Abstract No. 236142.

Andreozzi, G. B., Princivalle, F., Skogby, H., and Della Giusta, A. (2000). Cation ordering and structural variations with temperature in $MgAl_2O_4$ spinel: An X-ray single-crystal study. American Mineralogist, 85, 1164-1171.

Angel, R.J., Carpenter, M.A., and Finger, L.W. (1990). Structural variation associated with compositional variation and order-disorder behavior in anorthite-rich feldspars. American Mineralogist, 75, 150-162.

Angel, R.J., Gonzalez-Platas, J., and Alvaro, M. (2014) EosFit7c and a Fortran module (library) for equation of state calculations. Zeitschrift für Kristallographie - Crystalline Materials, 229, 405-419.

Ballirano, P., Celata, B., Skogby, H., Andreozzi, G.B., and Bosi, F. (2022) HT breakdown of Mn-bearing elbaite from the Anjanabonoina pegmatite, Madagascar. Journal of Geosciences, in press.

Berryman, E.J., Zhang, D., Wunder, B., and Duffy, T.S. (2019) Compressibility of synthetic Mg-Al tourmalines to 60 GPa, American Mineralogist, 104, 1005–1015.

Bosi, F., Skogby, H., and Hålenius, U. (2016) Thermally induced cation redistribution in Fe-bearing oxy-dravite and potential geothermometric implications. Contributions to Mineralogy and Petrology, 171, 47.

Bosi, F. (2018) Tourmaline crystal chemistry. American Mineralogist, 103, 298-306.

Bosi, F., Skogby, H., Hålenius, U., and Ciriotti, M. (2018) Experimental cation redistribution in the tourmaline lucchesiite, $CaFe^{2+}_3Al_6(Si_6O_{18})(BO_3)_3(OH)_3O$. Physics and Chemistry of Minerals, 45, 621–632.

Bosi, F., Skogby, H., and Hålenius, U. (2019) Thermally induced cation redistribution in fluor-elbaite and Fe-bearing tourmalines. Physics and Chemistry of Minerals, 46, 371-383.

Chernyshova, I.A., Vereshchagin, O.S., Frank-Kamenetskaya, O.V., Zolotarev, A.A., Krzhizhanovskaya, M.G., and Malyshkina, O.V. (2019) Thermal behavior and properties of synthetic Ni-bearing tourmaline. In XIX International meeting on crystal chemistry, X-ray diffraction and spectroscopy of minerals, p. 97-98.

Celata, B., Ballirano, P., Andreozzi, G.B., and Bosi, F. (2021) In situ high-temperature behaviour of fluor-elbaite: breakdown conditions and products. Physics and Chemistry of Minerals, 48, 24.

Dunn, P.J., Appleman, D.E., and Nelen, J.E. (1977) Liddacoatite, a new calcium end-member of the tourmaline group. American Mineralogist, 62, 1121-1124.

Dutrow, B.L., and Henry, D.J. (2011) Tourmaline: A geologic DVD. Elements, 7, 301–306.

Downs, R.T., and Hall-Wallace, H. (2003) The American Mineralogist crystal structure database. American Mineralogist, 88, 247-250.

Filatov, S. K., M. G. Gorskaya, and N. I. Bolotnikova (1987) Thermal deformations and phase transformations in tourmalines. Neorganiceskie materialy, 23.4, 594-599.

Filip, J., Bosi, F., Novák, M., Skogby, H., Tuček, J., Čuda, J., and Wildner M. (2012) Iron redox reactions in the tourmaline structure: High-temperature treatment of Fe3+-rich schorl. Geochimica et Cosmochimica Acta, 86, 239-256

Ganguly, J., Bose, J., and Ghose, S. (1989) Fe^{2+}-Mg ordering in orthopyroxenes and the cooling rates of meteorites. Lunar Planet Science Conference XX, 331-332.

Ganguly, J., and Domeneghetti, M. C. (1996). Cation ordering of orthopyroxenes from the Skaergaard intrusion: implications for the subsolidus cooling rates and permeabilities. Contributions to Mineralogy and Petrology, 122, 359-367.

Ghose, S. (1965) Mg^{2+}-Fe^{2+} order in an orthopyroxene, $Mg_{0.93}Fe_{1.07}Si_2O_6$. Zeitschrift fur Kristallographie, 122, 81-89.

Helme, B.G., and King, P.J. (1978) The elastic constants of iron tourmaline (schorl). Jourlan of Materials Science, 13, 1487–1489.

Hemingway, B.S., Evans, H.T., Mazdab, F.K. and Anovitz, L.M. (1996) Thermal expansion of some borate and borosilicate minerals (fluoborite, danburite, sinhalite, datolite, elbaite, dravite, kornerupine, dumortierite, ferro-axinite, and manganaxinite) between 25 and about 1200 °C. U.S. Geological Survey Open File Report, 96–100.

Henry, D.J., Novák, M., Hawthorne, F.C., Ertl, A., Dutrow, B.L., Uher, P., and Pezzotta, F. (2011) Nomenclature of the tourmaline-supergroup minerals. American Mineralogist, 96, 895–913.

Holland, T.J.B., and Redfern, S.A.T. (1997) Unit cell refinement from powder diffraction data: the use of regression diagnostics. Mineralogical Magazine, 61, 65–77.

Hovis, G.L., Medford, A., Conlon, M., Tether, A., and Romanoski, A. (2010) Principles of thermal expansion in the feldspar system. American Mineralogist, 95, 1060–1068. doi: https://doi.org/10.2138/am.2010.3484

Hovis, G.L., Tribaudino, M., Leaman, A., Almer, C., Altomare, C., Morris, M., Maksymiw, N., Morris, D., Jackson, K. Scott, B., Tomaino, G., and Mantovani, L. (2021) Thermal

expansion of minerals in the pyroxene system and examination of various thermal expansion models. American Mineralogist, 106, 883-899.

Kittel, C., McEuen, C., and McEuen, P. (1996) Introduction to solid state physics, 8th ed., 704 p. Wiley, New York.

Knight, K.S., and Price, G.D. (2008) Powder neutron-diffraction studies of clinopyroxenes. I: The crystal structure and thermoelastic properties of jadeite between 1.5 and 270 K. Canadian Mineralogist, 46, 1593–1622.

Kroll, H., Kirfel, A., Heinemann, R., and Barbier, B. (2012) Volume thermal expansion and related thermophysical parameters in the Mg, Fe olivine solid-solution series. European Journal of Mineralogy, 24, 935-956.

Ma, C., Tschauner, O., Beckett, J.R., Rossman, G.R., and Liu, W. (2012) Panguite, $(Ti^{4+},Sc,Al,Mg,Zr,Ca)_{1.8}O_3$, a new ultra-refractory titania mineral from the Allende meteorite: Synchrotron micro-diffraction and EBSD. American Mineralogist, 97, 1219-1225.

Molin, G.M., Domeneghetti, M.C., Salviulo, G., Stimpfl, M., and Tribaudino, M. (1994) Antarctic FRO90011 lodranite: cooling history from pyroxene crystal chemistry and microstructure. Earth and Planetary Science Letters, 128, 479-487.

O'Bannon, E., Beavers, C.M., Kunz, M., and Williams, Q. (2018) High-pressure study of dravite tourmaline: Insights into the accommodating nature of the tourmaline structure. American Mineralogist, 103, 1622-1633.

Pandey, C.S., and Schreuer, J. (2012) Elastic and piezoelectric constants of tourmaline single crystals at nonambient temperatures determined by resonant ultrasound spectroscopy. Journal of Applied Physics, 111, 013516.

Pandolfo, F., Cámara, F., Domeneghetti, C.M., Alvaro, M., Nestola, F., Karato, S., and Amulele, G. (2015) Volume thermal expansion along the jadeite-diopside join. Physics and Chemistry of Minerals, 42, 1-14.

Pina, C. M., Pimentel, C., and Crespo, Á. (2020). Dolomite cation order in the geological record. Chemical Geology, 547, 119667.

Pieczka, A., and Kraczka, J. (2004) Oxidized tourmalines - A combined chemical, XRD and Mössbauer study. European Journal of Mineralogy, 16, 309-321.

Pouchou, J.L., and Pichoir, F. (1991) Quantitative analysis of homogeneous or stratified microvolumes applying the model "PAP". In K.F.J. Heinrich and D.E. Newbury, Eds., Electron Probe Quantitation, p. 3l–75. Plenum Press

Redfern, S.A., Harrison, R.J., O'Neill, H.S.C., and Wood, D.R. (1999). Thermodynamics and kinetics of cation ordering in $MgAl_2O_4$ spinel up to 1600 C from in situ neutron diffraction. American Mineralogist, 84, 299-310.

Scribner, E.D., Cempírek, J., Groat, L.A., Evans, R.J., Biagioni, C., Bosi, F., Dini, A., Hålenius, U., Orlandi, P., and Pasero, M. (2021) Magnesio-lucchesiite, $CaMg_3Al_6(Si_6O_{18})(BO_3)_3(OH)_3O$, a new species of the tourmaline supergroup. American Mineralogist, 106, 862–871.

Tatli, A., and Pavlovic, A.S. (1988) Thermal expansion of tourmaline single crystals from 80 to 300 K. Physics Review B, Condensed Matter, 38, 10072–10074.

Tatli, A., and Özkan, H. (1987) Variation of the elastic constants of tourmaline with chemical composition. Physics and Chemistry of Minerals, 14, 172–176.

Tribaudino, M., Bruno, M., Iezzi, G., Della Ventura, G., and Margiolaki, I. (2008) The thermal behavior of richterite. American Mineralogist, 93, 1659–1665.

Tribaudino, M., Angel, R.J., Cámara, F., Nestola, F., Pasqual, D., and Margiolaki I. (2010) Thermal expansion of plagioclase feldspars. Contributions to Mineralogy and Petrology, 160, 899–908.

Tribaudino, M., Bruno, M., Nestola, F., Pasqual, D., and Angel, R.J. (2011) Thermoelastic and thermodynamic properties of plagioclase feldspars from thermal expansion measurements. American Mineralogist, 96, 992–1002.

Tribaudino M., and Mantovani L. (2014) Thermal expansion in *C*2/*c* pyroxenes: a review and new high temperature structural data on a pyroxene of composition $(Na_{0.53}Ca_{0.47})(Al_{0.53}Fe_{0.47})Si_2O_6$ ($Jd_{53}Hd_{47}$). Mineralogical Magazine, 78, 311-324

Tribaudino, M., Gatta, G.D., Aliatis, I., Bersani, D., and Lottici, P.P. (2018) Al/Si ordering in albite: A combined single-crystal X-ray diffraction and Raman spectroscopy study. Journal of Raman Spectroscopy, 49, 2028-2035.

Tribaudino, M., Hovis, G.L., Almer, C., and Leaman, A. (2022) Thermal expansion of minerals in the amphibole system. American Mineralogist, 107, 1302-1312. doi:10.2138/am-2022-7988

Watenphul, A., Malcherek, T., Wilke, F. D., Schlüter, J., and Mihailova, B. (2017) Composition–thermal expandability relations and oxidation processes in tourmaline studied by in situ Raman spectroscopy. Physics and Chemistry of Minerals, 44, 735-748.

Xu, J., Kuang, Y., Zhang, B., Liu, Y., Fan, D., Li, X., and Xie, H. (2016) Thermal equation of state of natural tourmaline at high pressure and temperature. Physics and Chemistry of Minerals, 43, 315-32.

FIGURE CAPTIONS

Figure 1: Crystal structure of tourmaline: a) along the b axis and b) parallel to the c axis.

Figure 2: Thermal expansion of Na-rich rossmanite (formerly elbaite) GRR 916b compared with the high-T elbaite data of Ballirano et al. (2022) and Hemingway et al. (1996).

Figure 3: Thermal expansion coefficient vs. temperature in Na-rich rossmanite and schorl. The coefficient was calculated from the fit reported in Table 3.

Figure 4: Plots of high-temperature divided by room-temperature unit-cell parameters for present samples. Lines connect experimental measurements (symbols omitted for clarity). a) Upper left: thermal expansion of Li- and Fe^{2+}-free samples (fluor-liddicoatite added in bold for reference). b) Upper right: Thermal expansion of Li-rich tourmalines (data for □-rich dravite added for reference, fluor-liddicoatite in bold). c) Lower left: Thermal expansion of the Fe^{2+}-rich tourmalines compared with that for dravite. Thermal behavior of Fe^{2+}-rich fluor-elbaite from Celata et al. (2021) is shown for comparison.

Figure 5: Elbaite thermal expansion: Dilatometric data were calibrated against room temperature value of elbaite FH AT31. The data from elbaite were scaled to overlap with those for Na-rich rossmanite (GRR 916). The line is not a fit, but rather the thermal expansion from Pandley and Schreurer (2012), sample T003.

Figure 6: Povondraite unit cells compared with those for □-rich dravite NMNH 78719-1.

Figure 7: Thermal expansion along the a and c crystallographic axes. Thermal expansion according to the Fei model, fit over the range reported in Table 3.

Figure 8: Volume thermal expansion coefficient vs. axial expansion along a; data are from the FEI model at 298K.

Figure 9: Thermal expansion variability in mineral supergroups: Pyroxene and amphibole data are from Hovis et al. (2021) and Tribaudino et al. (2022), respectively, with tourmaline data from the present work. The box represents the upper and lower 25 and 75 % of the data, whereas the line in between is the median; whiskers represent the minimum and maximum values.

This is the peer-reviewed, final accepted version for American Mineralogist, published by the Mineralogical Society of America.
The published version is subject to change. Cite as Authors (Year) Title. American Mineralogist, in press.
DOI: https://doi.org/10.2138/am-2022-8580. http://www.minsocam.org/

TABLES

MODIFIED TOURMALINE NAME	NAME AT SAMPLE SOURCE	SAMPLE NUMBER[1]	LOCALITY	X	
				Na	**Ca**
dravite	dravite	NMNH 103791-1	Dobrowa, Carinthia, Austria	0.79	0
□-rich dravite	dravite	NMNH 78719-1	Gouverneur, St. Lawrence Co., NY, USA	0.5	0
Fe-rich fluor-elbaite	fluor-schorl	FH T21	San Diego Co., CA, USA	0.88	0.01
schorl	schorl	NMNH 118462	Fitchburg, Worcester Co., MA, USA	0	0.1
Na-rich rossmanite	elbaite	GRR 916	Himalaya Mine, near Mesa Grande, San Diego Co., CA, USA	0.43	0
elbaite	elbaite	FH AT31	Belo Horizonte, Brazil	0.62	0.06
□-rich elbaite	rossmanite	GRR 2361	Tanco Mine, Bernic Lake, Manitoba, Canada	0.53	0.04
fluor-buergerite	buergerite	NMNH R12583	Mexquitic, San Luis Potosi, Mexico	0.8	0.16
fluor-liddicoatite	liddacoatite	FH AT20/NT7	Namibia	0.19	0.75
Na-rich foitite	foitite	GRR 794	Schindler Deposit, Cahuilla Mountain, Riverside, CA, USA	0.43	0.01
□-Al-B-rich elbaite	olenite	FH AT51/BH17	Nina La Verde, Brazil	0.52	0.08
Na-Fe-rich fluor-uvite	uvite	FH T95/CT72	Mt. Isa, Queensland, Australia	0.31	0.66
fluor-uvite	uvite	NMNH B14687	Franklin, Sussex Co., NJ, USA	0.03	1.02
Na-rich fluor-uvite	fluor-uvite	GRR 2396	Kenya	0.32	0.62

1. Sample sources include the U.S. National Museum of Natural History (NMNH), Frank Hawthorne (FH), and

This is the peer-reviewed, final accepted version for American Mineralogist, published by the Mineralogical Society of America.
The published version is subject to change. Cite as Authors (Year) Title. American Mineralogist, in press.
DOI: https://doi.org/10.2138/am-2022-8580. http://www.minsocam.org/

Table 1: Sample information. Note that data from analyses at the sample origin have been recalculated. Names given in column 1 utilize the classification scheme of Henry et al. (2011). X through W refer to atom position in the tourmaline general formula. □ refers to vacancies.

	Weight %
SiO_2	30.92(62)
TiO_2	0.23(77)
B_2O_3[a]	8.89
Al_2O_3	3.11(1.89)
Fe_2O_3[b]	43.96(3.04)
MgO	5.96(50)
CaO	0.07(20)
Na_2O	2.13(19)
K_2O	0.86(22)
F	0.03(4)
H_2O[a]	1.99
$–O \equiv F$	–0.01
Total	98.13

[a] Calculated from stoichiometry.
[b] Determined by Mössbauer spectroscopy.
Notes: Uncertainties for oxides and fluorine (in brackets) are standard deviations of 117 spots. The unusual standard deviations for constituents such as CaO are the result of non-Gaussian data distributions for the latter.

Table 2: Chemical compositions of povondraite AMNH 110379.

This is the peer-reviewed, final accepted version for American Mineralogist, published by the Mineralogical Society of America.
The published version is subject to change. Cite as Authors (Year) Title. American Mineralogist, in press.
DOI: https://doi.org/10.2138/am-2022-8580. http://www.minsocam.org/

Mineral	Sample name	Sample Number	k'	θ_E (K)	V_0
schorl	schorl	NMNH 118462	4	407(17)	15
elbaite	elbaite	FH AT31	4	487(16)	15
Na-rich rossmanite	elbaite	GRR 916	4	521(14)	15
fluor-uvite	uvite	NMNH B14687	4	594(22)	15
Na-Fe-rich fluor-uvite	uvite	FH T95	4	506(23)	15

Table 3: Fitted parameters according to the Kroll physical equation. Data from 80 to 300K are from Tatli and Pavlovic (1988); higher-temperature data are in the range reported in Table 4.

This is the peer-reviewed, final accepted version for American Mineralogist, published by the Mineralogical Society of America.
The published version is subject to change. Cite as Authors (Year) Title. American Mineralogist, in press.
DOI: https://doi.org/10.2138/am-2022-8580. http://www.minsocam.org/

Sample name	Sample number	T (K)	$V_{0,298K}$ (Å^3)	$^2a_0$	a_1	$\alpha_{V,298}$
dravite	NMNH 103791-1	298-1101	1580.94(14)	1.82(8)	0.75(11)	2.0
□-rich dravite	NMNH 78719-1	298-1051	1598.36(8)	1.98(10)	0.59(15)	2.1
Fe-rich fluor-elbaite	FH T21	298-951	1563.73(14)	1.73(14)	0.78(23)	1.9
schorl	NMNH 118462	298-801	1584.90(12)	1.62(15)	0.89(28)	1.8
Na-rich rossmanite	GRR 916	298-901	1540.55(6)	1.61(6)	1.22(11)	1.9
elbaite	FH AT31	298-801	1543.27(12)	1.46(16)	1.45(29)	1.9
□-rich elbaite	GRR 2361	298-995	1538.95(7)	1.76(6)	0.98(10)	2.0
fluor-buergerite	NMNH R12583	298-1101	1567.75(12)	2.09(7)	0.31(9)	2.1
fluor-liddicoatite	FH AT20	298-1101	1544.43(12)	2.03(8)	0.60(11)	2.2
Na-rich foitite	GRR 794	298-645	1579.70(8)	1.67(19)	0.83(48)	1.9
□-Al-B-rich elbaite	FH AT51 (= BH17)	298-951	1525.72(7)	1.63(10)	1.01(19)	1.9
Na-Fe-rich fluor-uvite	NMNH B14687	298-951	1590.42(13)	1.53(11)	1.2517)	1.9
fluor-uvite	FH T95	298-801	1587.16(9)	1.56(11)	1.11(21)	1.8
Na-rich fluor-uvite	GRR 2396	298-1151	1576.59(9)	1.90(5)	0.66(6)	2.1
povondraite	[1]MGMH 134842	298-1045	1711.51(63)	1.84(24)	0.63(55)	2.0

Table 4: Fitted parameters according to the Fei empirical equation, with a_0, a_1 and α_{298K} to be multiplied by 10^{-5}, 10^{-8} and 10^{-5}, respectively.

This is the peer-reviewed, final accepted version for American Mineralogist, published by the Mineralogical Society of America.
The published version is subject to change. Cite as Authors (Year) Title. American Mineralogist, in press.
DOI: https://doi.org/10.2138/am-2022-8580. http://www.minsocam.org/

FIGURES

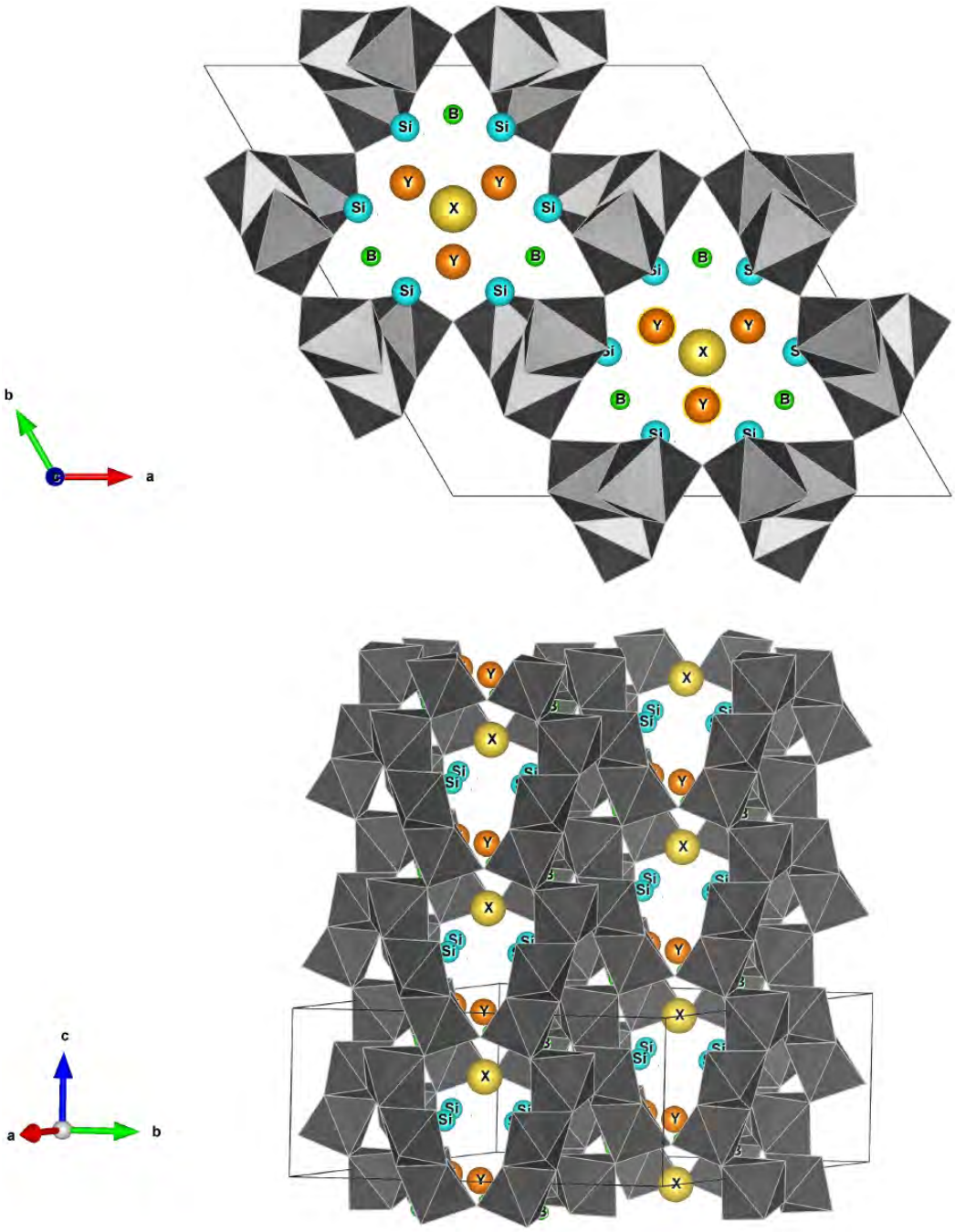

Figures 1a (top) and 1b (bottom)

This is the peer-reviewed, final accepted version for American Mineralogist, published by the Mineralogical Society of America.
The published version is subject to change. Cite as Authors (Year) Title. American Mineralogist, in press.
DOI: https://doi.org/10.2138/am-2022-8580. http://www.minsocam.org/

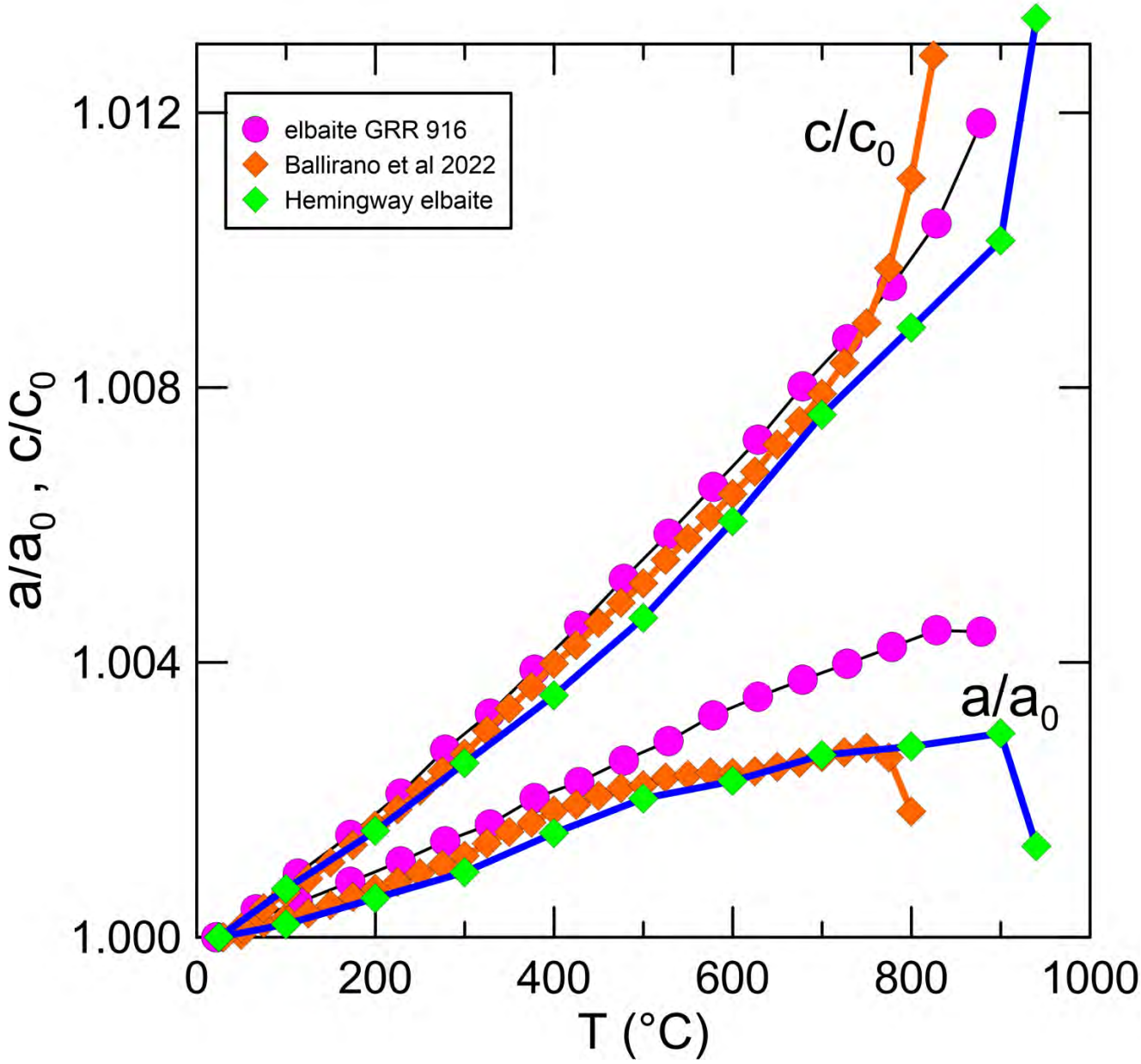

Figure 2

This is the peer-reviewed, final accepted version for American Mineralogist, published by the Mineralogical Society of America.
The published version is subject to change. Cite as Authors (Year) Title. American Mineralogist, in press.
DOI: https://doi.org/10.2138/am-2022-8580. http://www.minsocam.org/

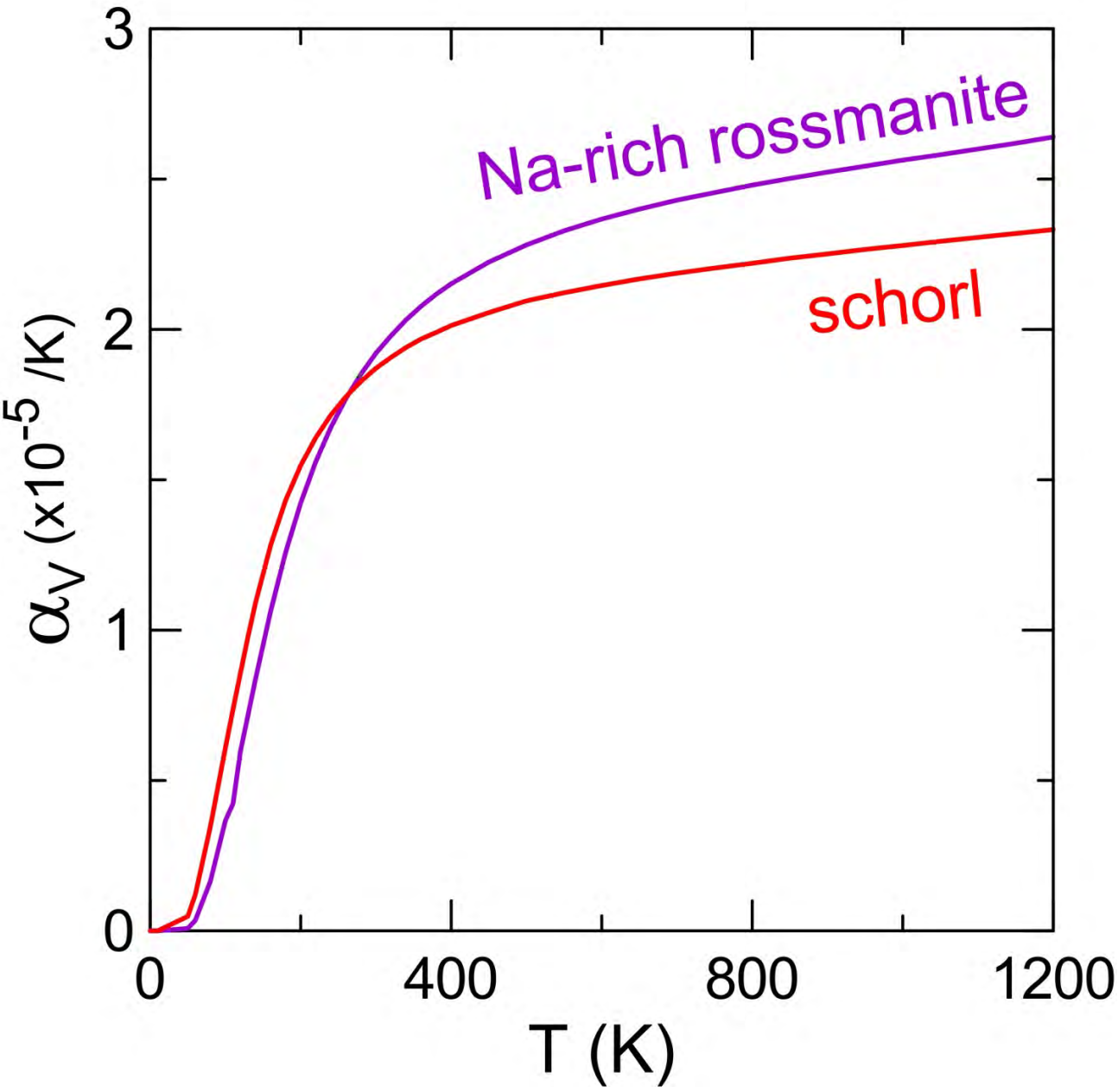

Figure 3

This is the peer-reviewed, final accepted version for American Mineralogist, published by the Mineralogical Society of America.
The published version is subject to change. Cite as Authors (Year) Title. American Mineralogist, in press.
DOI: https://doi.org/10.2138/am-2022-8580. http://www.minsocam.org/

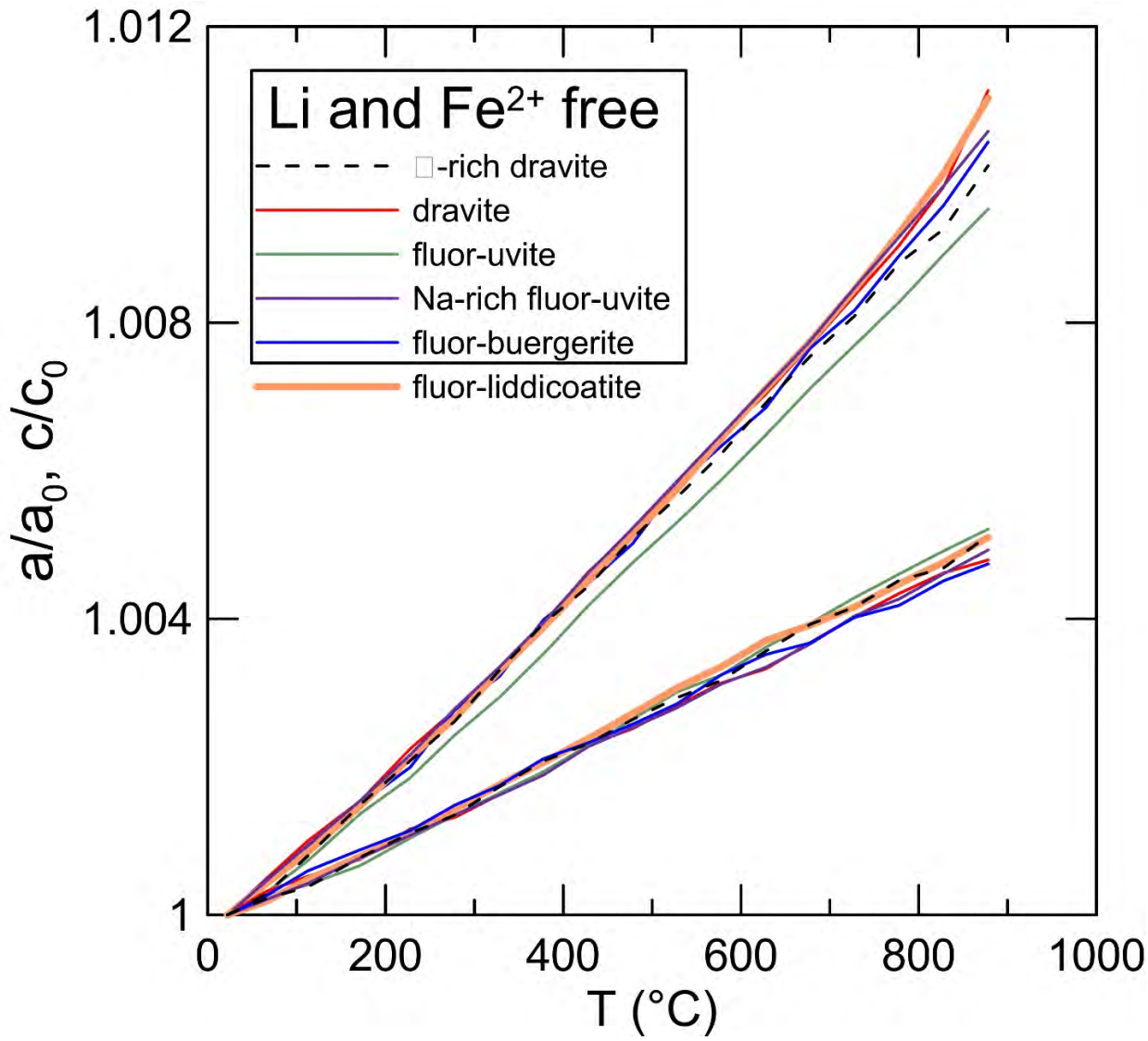

Top left diagram of Figure 4; figure continued next page

This is the peer-reviewed, final accepted version for American Mineralogist, published by the Mineralogical Society of America.
The published version is subject to change. Cite as Authors (Year) Title. American Mineralogist, in press.
DOI: https://doi.org/10.2138/am-2022-8580. http://www.minsocam.org/

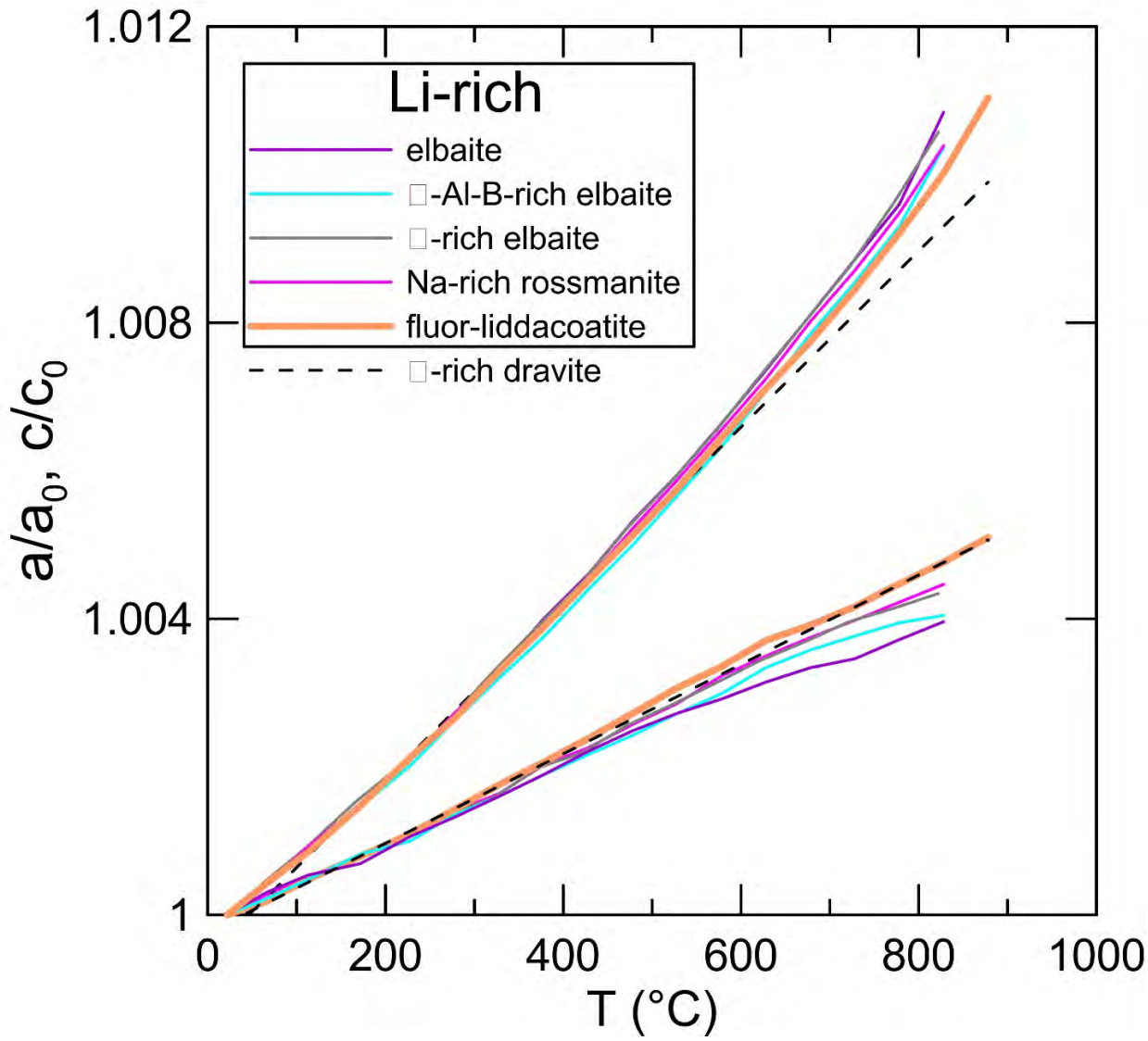

Top right diagram of Figure 4, figure continued next page

This is the peer-reviewed, final accepted version for American Mineralogist, published by the Mineralogical Society of America.
The published version is subject to change. Cite as Authors (Year) Title. American Mineralogist, in press.
DOI: https://doi.org/10.2138/am-2022-8580. http://www.minsocam.org/

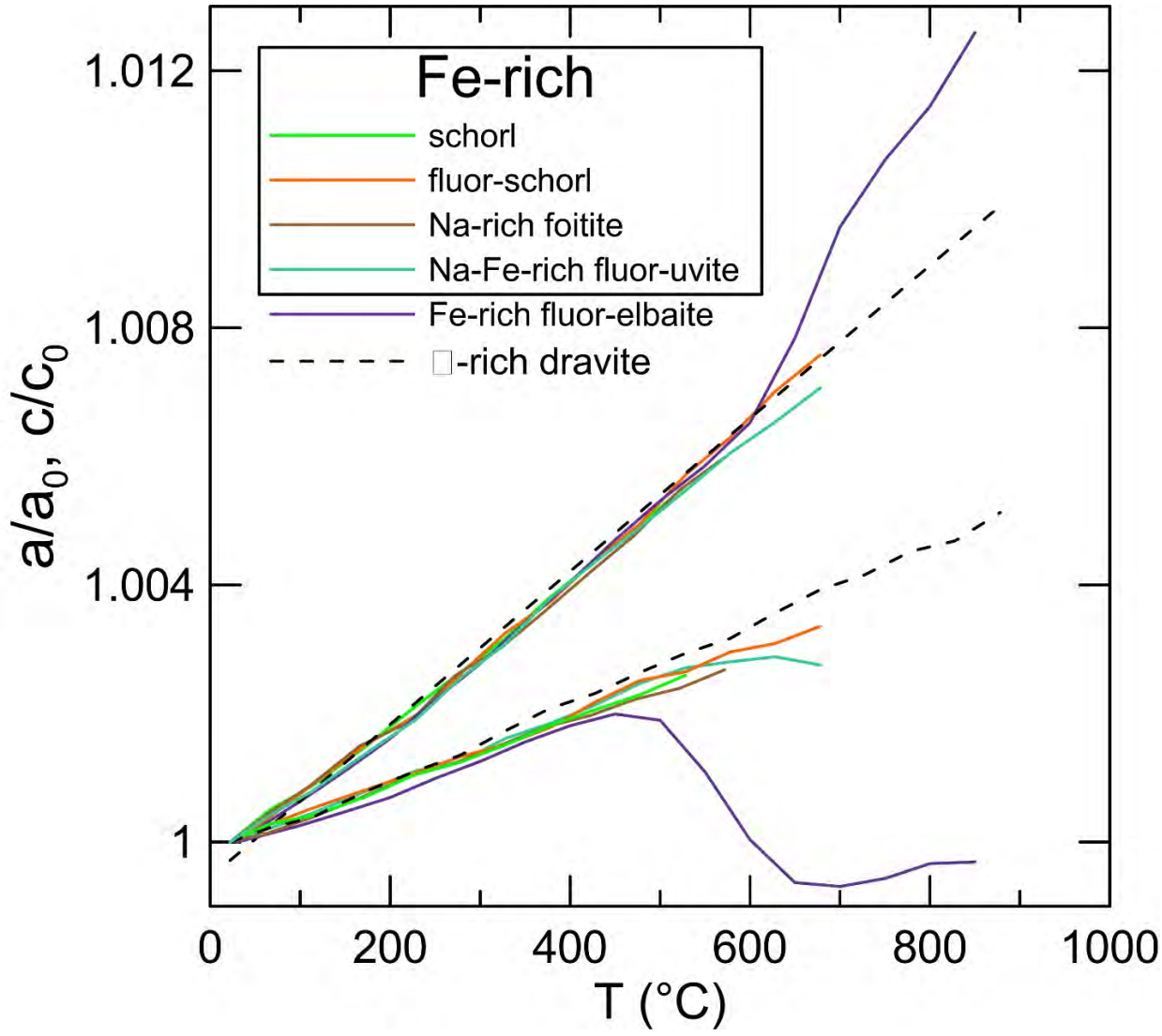

Bottom left diagram of Figure 4 (end of Figure 4)

This is the peer-reviewed, final accepted version for American Mineralogist, published by the Mineralogical Society of America.
The published version is subject to change. Cite as Authors (Year) Title. American Mineralogist, in press.
DOI: https://doi.org/10.2138/am-2022-8580. http://www.minsocam.org/

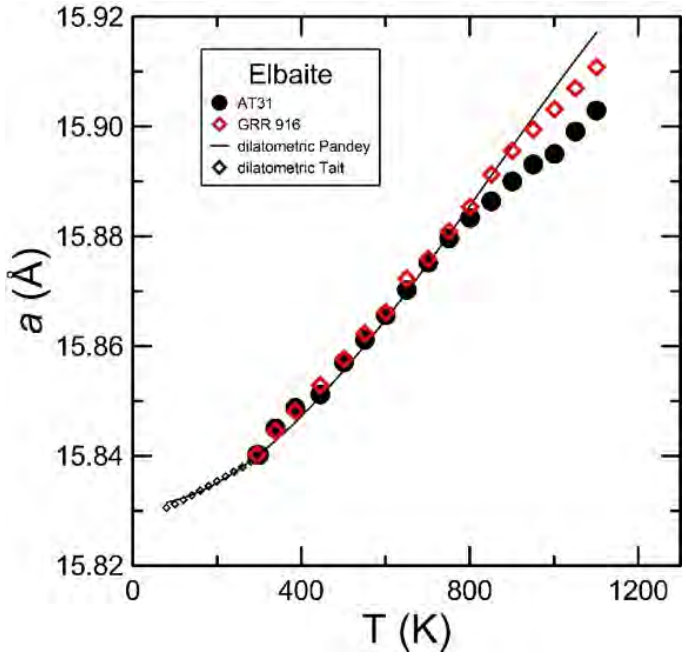

Top left diagram of Figure 5

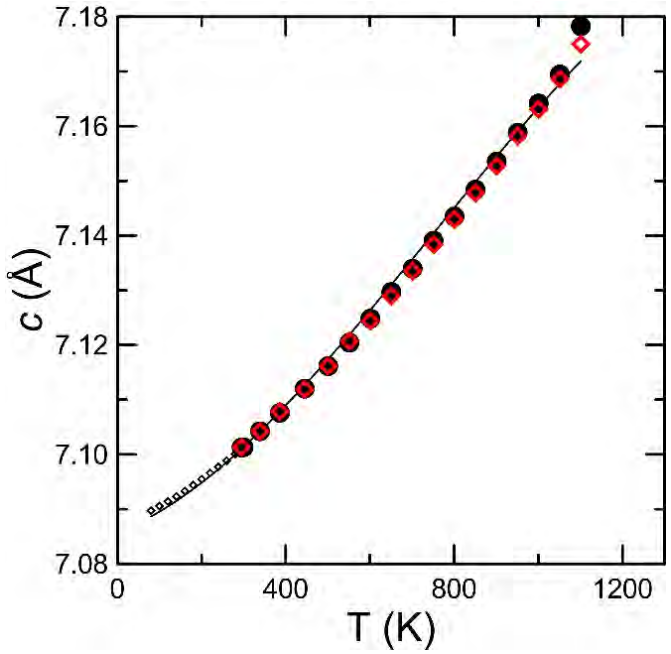

Top right diagram of Figure 5, figure continued next page

This is the peer-reviewed, final accepted version for American Mineralogist, published by the Mineralogical Society of America.
The published version is subject to change. Cite as Authors (Year) Title. American Mineralogist, in press.
DOI: https://doi.org/10.2138/am-2022-8580. http://www.minsocam.org/

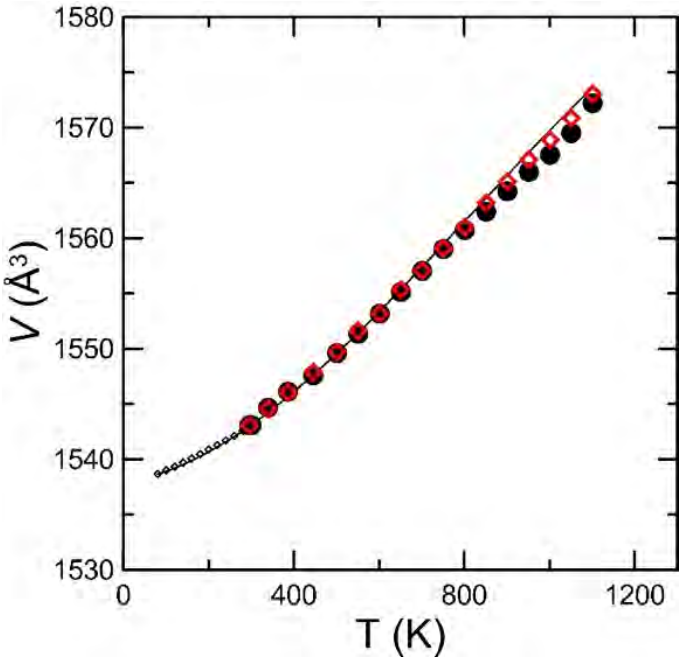

Bottom left diagram of Figure 5 (end of Figure 5)

This is the peer-reviewed, final accepted version for American Mineralogist, published by the Mineralogical Society of America.
The published version is subject to change. Cite as Authors (Year) Title. American Mineralogist, in press.
DOI: https://doi.org/10.2138/am-2022-8580. http://www.minsocam.org/

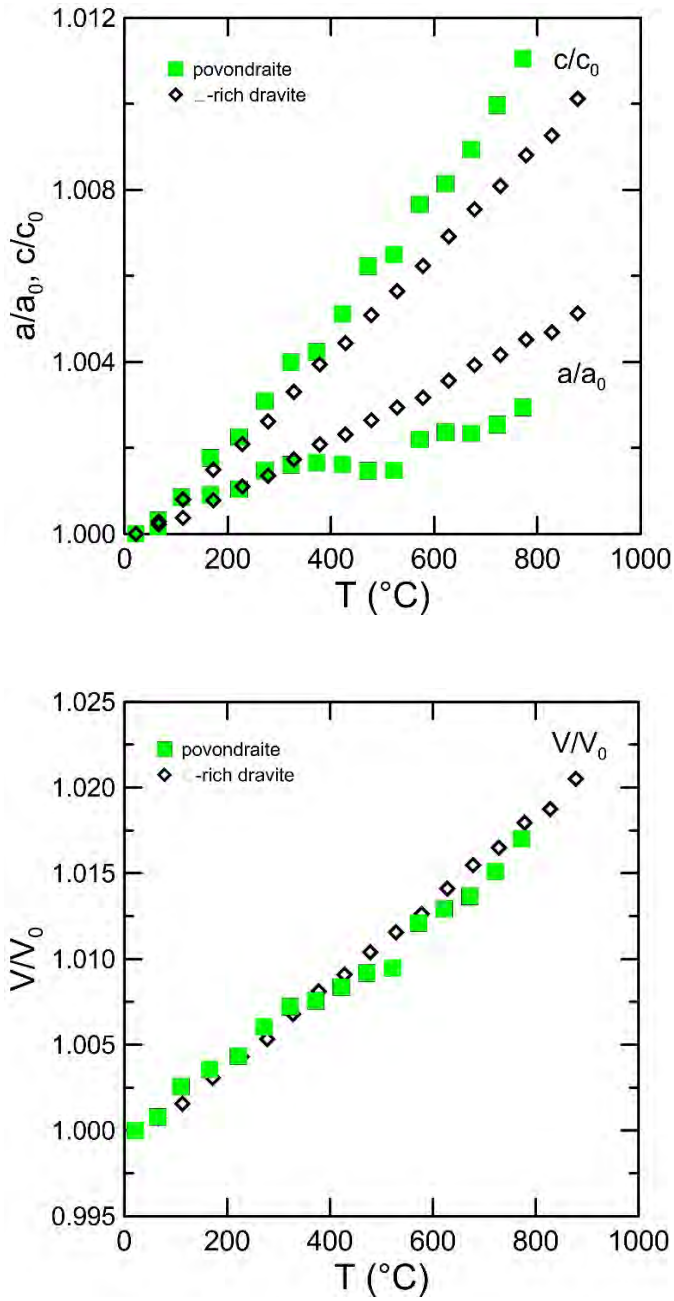

Figure 6

This is the peer-reviewed, final accepted version for American Mineralogist, published by the Mineralogical Society of America.
The published version is subject to change. Cite as Authors (Year) Title. American Mineralogist, in press.
DOI: https://doi.org/10.2138/am-2022-8580. http://www.minsocam.org/

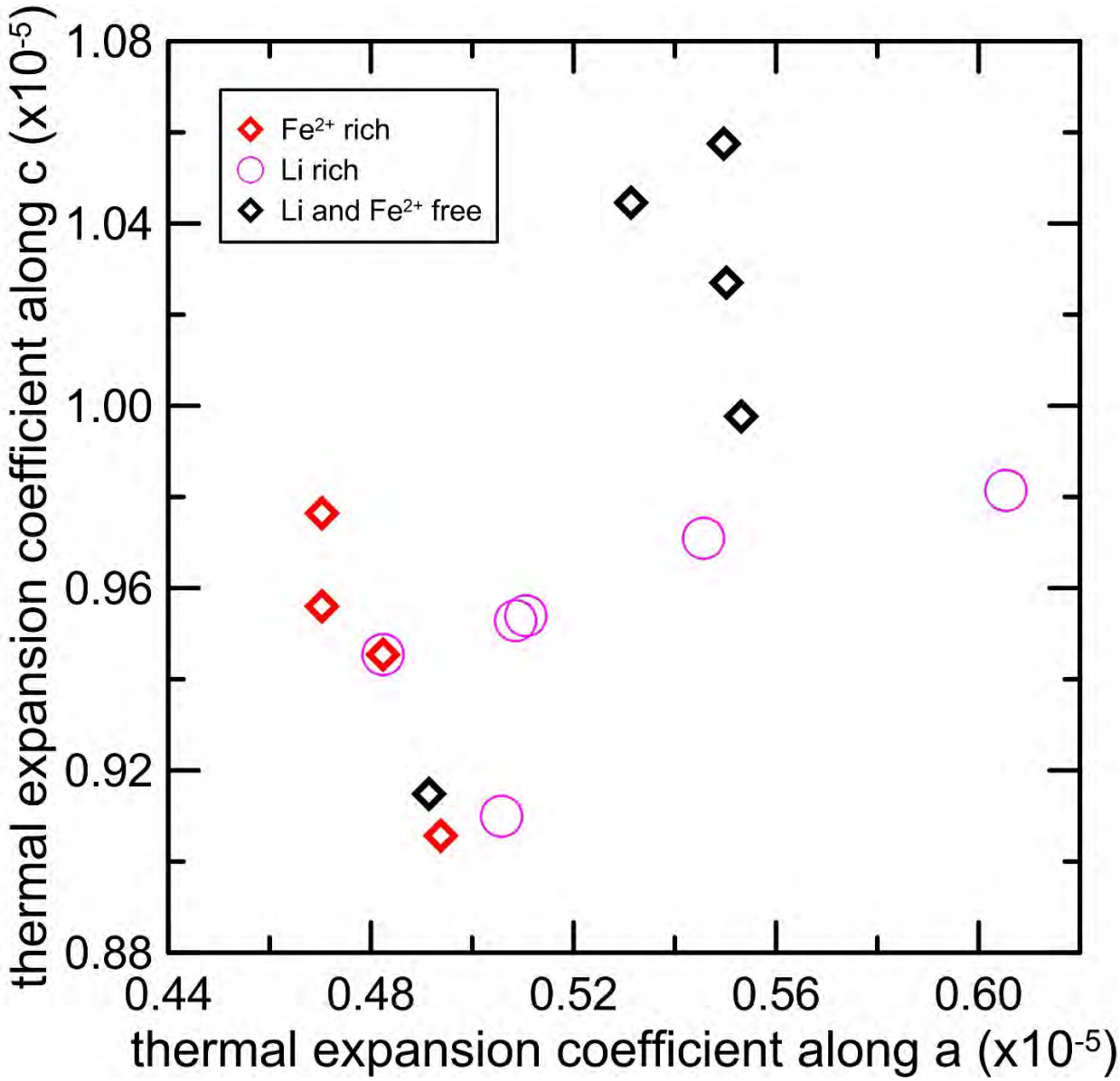

Figure 7

This is the peer-reviewed, final accepted version for American Mineralogist, published by the Mineralogical Society of America.
The published version is subject to change. Cite as Authors (Year) Title. American Mineralogist, in press.
DOI: https://doi.org/10.2138/am-2022-8580. http://www.minsocam.org/

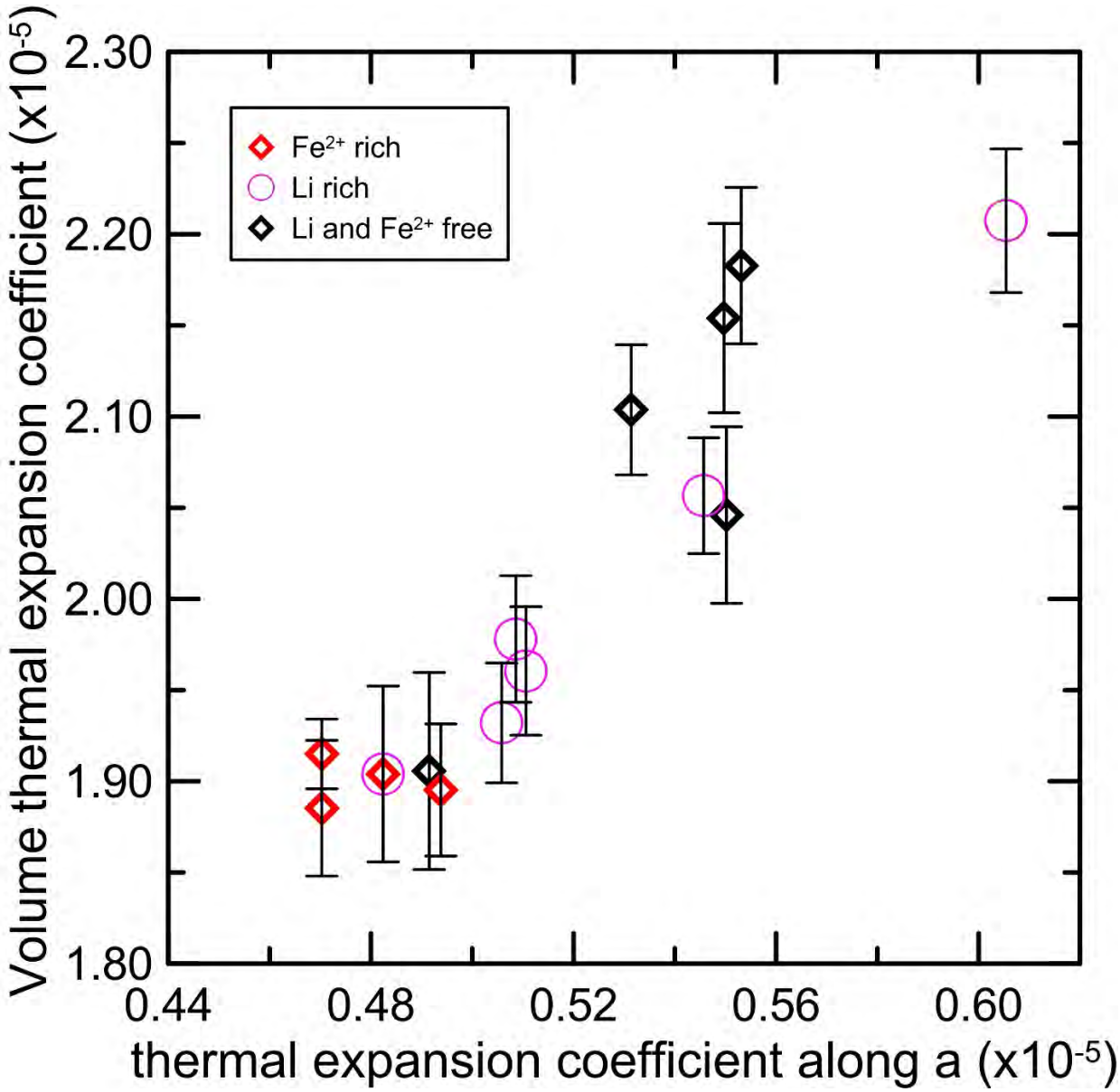

Figure 8

This is the peer-reviewed, final accepted version for American Mineralogist, published by the Mineralogical Society of America.
The published version is subject to change. Cite as Authors (Year) Title. American Mineralogist, in press.
DOI: https://doi.org/10.2138/am-2022-8580. http://www.minsocam.org/

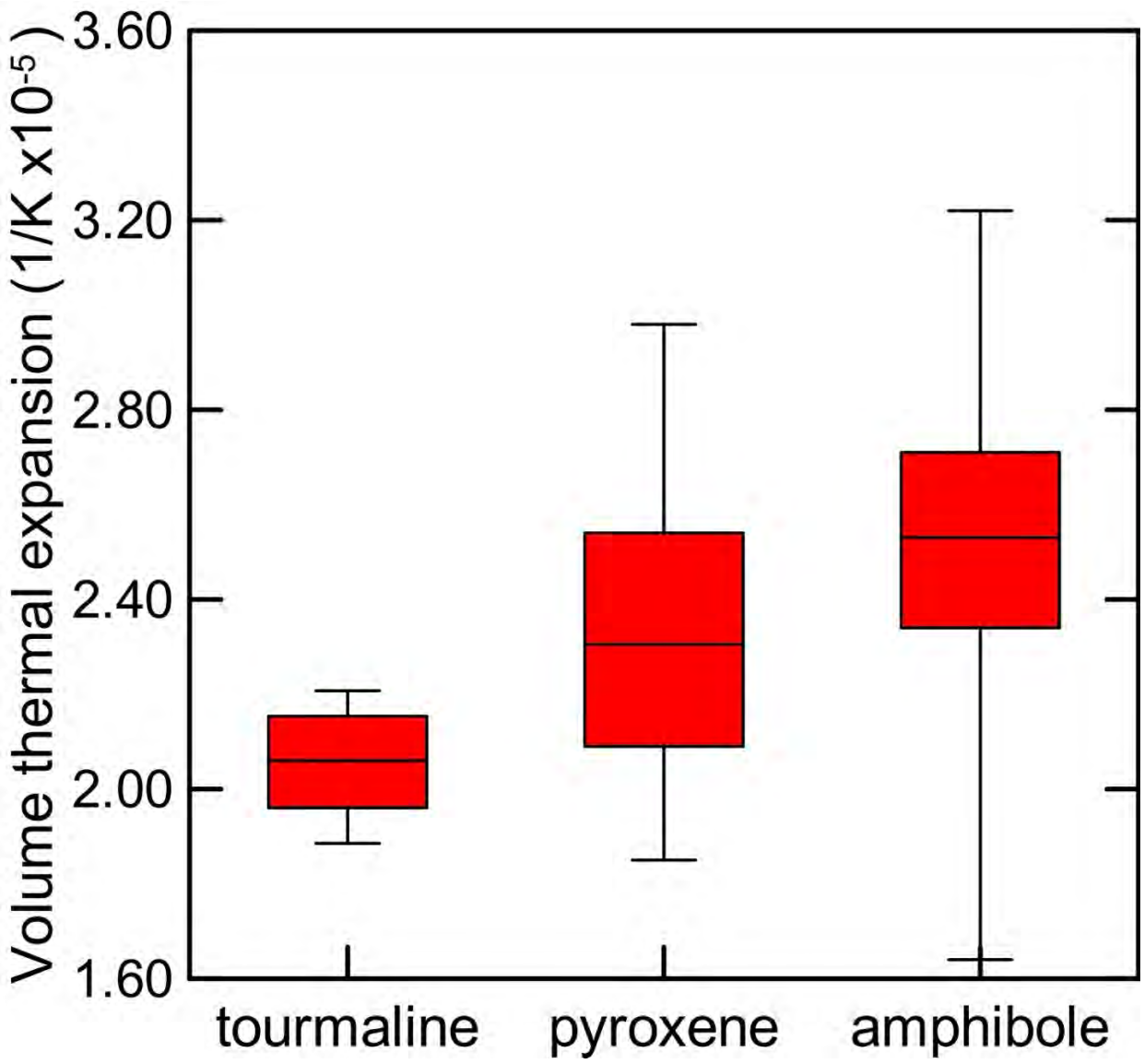

Figure 9

This is the peer-reviewed, final accepted version for American Mineralogist, published by the Mineralogical Society of America.
The published version is subject to change. Cite as Authors (Year) Title. American Mineralogist, in press.
DOI: https://doi.org/10.2138/am-2022-8580. http://www.minsocam.org/

Table 3: Fitted parameters according to the Kroll physical equation. Data from 80 to 300K are fro

Mineral	Sample name	Sample Number	k'	θ_E (K)	$V_{0,\,298K}$ (Å^3)
schorl	schorl	NMNH 118462	4	407(17)	1584.86(4)
elbaite	elbaite	FH AT31	4	487(16)	1543.22(6)
Na-rich rossmanite	elbaite	GRR 916	4	521(14)	1540.52(5)
fluor-uvite	uvite	NMNH B14687	4	594(22)	1590.58(7)
Na-Fe-rich fluor-uvite	uvite	FH T95	4	506(23)	1587.30(7)

m Tatli and Pavlovic (1988); higher-temperature data are in the range reported in Table 4.

$\alpha_{V,\ 298K}$ (1/K)	$\alpha_{V,\ 1000K}$ (1/K)	Fe^{2+}	Li
1.86(1)	2.28(1)	2.02	0
1.91(1)	2.48(1)	0.12	1.13
1.91(1)	2.56(1)	0	0.7
1.77(2)	2.52(1)	0.01	0
1.79(2)	2.35(2)	0.64	0.08